THE ASTROPHYSICAL JOURNAL, 429:645–671, 1994 July 10

STATISTICAL ANALYSIS OF TURBULENCE IN MOLECULAR CLOUDS

MARK S. MIESCH[1] AND JOHN BALLY[2]
Center for Astrophysics and Space Astronomy, Department of Astrophysical, Planetary, and Atmospheric Sciences, University of Colorado, Campus Box 389, Boulder, CO 80309
Received 1993 September 15; accepted 1993 December 3

ABSTRACT

We present an investigation of the statistical properties of fluctuating gas motions in five nearby molecular clouds using the two-point autocorrelation and structure functions and the power spectra of their radial velocity structure as traced by emission-line centroid velocities. Our analysis includes observations made with the AT&T Bell Laboratories 7 m Crawford Hill antenna (1.'7 beamwidth) of ^{13}CO $J = 1 \rightarrow 0$ emission in Orion B, Mon R2, L1228, and L1551 and also ^{13}CO $J = 2 \rightarrow 1$ observations of the molecular gas surrounding the Herbig-Haro object HH 83 lying just west of L1641 in the Orion A cloud that were obtained with a higher spatial resolution (0.'22) using the IRAM-30 m telescope on Pico Veleta, Spain. The effects of beam smoothing and the interpolation of a set of observations onto a regular spatial grid are studied using model spectral line data cubes, and we find that the behavior of the statistical functions presented here and those presented elsewhere by other authors are heavily influenced by these effects at scales comparable to and somewhat larger than the beamwidth. At larger lags real correlations are detected, and we use the e-folding length of the autocorrelation function (i.e., the correlation length) to investigate the characteristic scales of the underlying turbulent flow. We find that this measure is dependent on the range of scales sampled by the observations themselves both for our data and for previously existing observations presented by other authors, and we interpret this result and the observed similarity between the functional forms of the statistical functions derived for different data sets as evidence for a self-similar turbulent hierarchy of gas motions extending over a wide range of scales in the interstellar medium. Power-law fits to the observed structure functions yield a mean index describing the hierarchy of 0.86 ± 0.3, which translates into a velocity dispersion–region size relationship of the type first introduced by Larson (1981), $\Delta V \propto l^{\gamma}$, with $\gamma = 0.43 \pm 0.15$. This result is consistent with that found by Larson in his original analysis, $\gamma \approx 0.38$, and with the range found in more recent studies, $0.35 < \gamma < 0.7$. We also discuss the observed scaling laws in relation to the predictions of phenomenological theories of forced, isotropic turbulence. The mean turbulent stress and maximum energy transport rate as a function of scale are obtained from the velocity power spectra following the procedure of Kleiner & Dickman, and the results are discussed in the context of scale-dependent star formation and the generation of turbulence in molecular clouds.

Subject headings: ISM: clouds — ISM: molecules — turbulence

1. INTRODUCTION

Gas motions in the interstellar medium in general and molecular clouds in particular are typically characterized by very large Reynolds numbers, a high degree of nonlinearity in the governing equations, and complicated coupling and feedback mechanisms linking a variety of physical processes occurring over a wide range of scales (Scalo 1987). For these reasons, it is expected on theoretical grounds that the kinematics of molecular clouds should be sufficiently complex to warrant a description in terms of turbulent flow. Observationally, it has been suggested that the supersonic emission-line widths exhibited by most molecular clouds, the emission-line centroid velocity fluctuations found both in the Galaxy and in the LMC (§ 2), the complicated, filamentary, and possibly fractal nature of molecular cloud column density structure (Chappell & Scalo 1993; Falgarone, Phillips, & Walker 1991; Henriksen 1991), and the now well-established scaling relations between average velocity dispersion and cloud size (see Myers 1987 and references therein) can all be attributed to turbulence in some form. Although there are other interpretations, it is at least likely that gas motions in molecular clouds possess some turbulent component, which could have a profound influence on the details of the star formation process on all scales, from the localized gravitational collapse and fragmentation of a protostellar cloud (e.g., Léorat, Passot, & Pouquet 1990) to the global phenomena giving rise to galaxy-wide starbursts. It is therefore important to characterize the nature of the velocity and density structure typical of molecular clouds through observation in order to provide the initial conditions and physical insight necessary for relevant hydrodynamical simulations and realistic star formation theories.

Turbulence, virtually by definition, is inherently stochastic (or at least inhabits a high-dimensional deterministic attractor).[3] Flow variables such as velocity and density will fluctuate in an unpredictable manner about their mean values, and any attempt to follow quantitatively their time evolution and spatial structure must therefore be statistical. However, any real flow is not *entirely* random, and is instead characterized by a number of length scales and scaling laws (e.g., Tennekes & Lumley 1972), and a useful way to investigate the multiscale properties of the flow, and in turn the energetics and dynamics of the turbulence, is through two-point statistical functions such as the autocorrelation function (ACF), the structure function (SF), and the frequency-space analog of the

[1] miesch@janos.colorado.edu.
[2] bally@janos.colorado.edu.

[3] We thank J. M. Scalo for pointing this qualification out.

ACF, the power spectrum (PS) (§ 2.1). These diagnostics are less ambiguous than the size–line width scaling relations mentioned above and can, in principle, provide more information on the nature of the turbulence (Dickman 1985; Scalo 1984).

We present an analysis based on the PS and two-point ACF and SF of velocity fluctuations in a selection of nearby molecular clouds as traced by the velocity centroids of ^{13}CO $J = 1 \rightarrow 0$ emission lines (with the exception of HH 83, which were data taken in the ^{13}CO $J = 2 \rightarrow 1$ transition; see § 3.1). Our survey covers Orion B, Mon R2, L1228, L1551, and a smaller field to the west of L1641 in the Orion A cloud (the HH 83 molecular cloud; see Bally, Castets, & Duvert 1994), and it represents the most extensive application to date (in terms of the size of the data set) of the correlation function approach to the analysis of interstellar turbulence. We find that the turbulent length scales derived from the statistical functions for a particular set of observations are dependent on the range in scales sampled by the observations themselves, and interpret these and other existing correlation results for gas motions in the ISM as evidence for the existence of a turbulent hierarchy extending to larger and smaller scales. We discuss the observed scaling laws of the hierarchy in terms of existing phenomenological predictions for isotropic turbulence and in relation to the region size-velocity dispersion relations first noticed by Larson (1981) and more recently reviewed by Myers (1987). The variation of turbulent pressure and latent energy dissipation with region size is also presented and interpreted in the context of scale dependent star formation. Finally, energy injection mechanisms are reviewed and discussed in terms of the generation of turbulence in molecular clouds. The statistical approach will be presented in § 2, followed by a description of the observations themselves in § 3 and the application of the statistical analysis to the ^{13}CO maps in § 4. In the final sections (§ 5 and 6), we will provide an interpretation of our results and some concluding remarks.

2. STATISTICAL ANALYSIS

Although the lowest-order statistical functions do not provide a very complete description of a turbulent flow, they can be useful diagnostics, and as such, two point correlation functions, structure functions, and power spectra have been used frequently in the astronomical literature as a tool for understanding fluctuating gas motions in molecular clouds (Kleiner & Dickman 1984, 1985, and 1987; Dickman & Kleiner 1985; Scalo 1984; Hobson 1992; Kitamura et al. 1993; Pérault, Falgarone, & Puget 1986), H II regions (Roy & Joncas 1985; Roy, Arsenault, & Joncas 1986; O'Dell 1986; O'Dell & Castañada 1987; Castañeda 1988), and neutral hydrogen in the Large Magellanic Cloud (Spicker & Feitzinger 1988a, b). Similar approaches have also been applied to scintillation measurements toward pulsars and other radio sources (Rickett 1988; Narayan 1988), which are thought to sample turbulence in the ionized phases of the ISM (Higdon 1984). The present work will follow closely the statistical analysis of emission-line centroid velocity fluctuations in molecular clouds developed by Dickman & Kleiner (1985, hereafter DK 1985), Kleiner & Dickman (1987, hereafter KD 1987), and Spicker & Feitzinger (1988b, hereafter SF 1988b). We will only review their methods here, and the reader is referred to those papers for a more detailed discussion.

2.1. *Two-Point Statistics*

The application of statistical methods to investigate the velocity structure of molecular clouds is in practice limited to a time-independent, spatially two-dimensional analysis of radial velocity fluctuations on the plane of the sky (e.g., Dickman 1985). The mean radial velocity of emitting gas averaged over the depth of the cloud is given by the velocity centroid of an emission line if the cloud is homogeneous and the emission is optically thin. For an inhomogeneous cloud the measured centroid velocity will change with excitation temperature and opacity variations along the line of sight, but Dickman & Kleiner (1985) show that these effects vanish to first order, and therefore the centroid of an optically thin emission line will closely approximate the mean radial velocity of the gas averaged over the emitting region. Although molecular cloud cores are not thought to be transparent to ^{13}CO $J = 1 \rightarrow 0$ emission (Castets et al. 1990), the cloud envelopes are, and since most of the gas traced in our observations belongs to the envelopes, the optically thin assumption is not too much in error. Furthermore, even when the optical depth exceeds unity, the observed centroid fluctuations will probe velocity structure deep within the cloud if the emission comes from the surfaces of discrete clumps with different radial velocities (Hobson 1992), or if the line wings, which contribute more than the line cores to the centroid velocity calculation, are optically thin (Kitamura et al. 1993).

We define the discrete, two-dimensional spatial autocorrelation function and structure function as follows;

$$C(\boldsymbol{\tau}) \equiv \frac{\sum [v_c(\boldsymbol{r}) - \mu][v_c(\boldsymbol{r} + \boldsymbol{\tau}) - \mu]}{\sigma_c^2 N(\boldsymbol{\tau})} \tag{1}$$

and

$$S(\boldsymbol{\tau}) \equiv \frac{\sum [v_c(\boldsymbol{r}) - v_c(\boldsymbol{r} + \boldsymbol{\tau})]^2}{\sigma_c^2 N(\boldsymbol{\tau})}, \tag{2}$$

with the mean centroid velocity denoted as

$$\mu \equiv \frac{\sum v_c(\boldsymbol{r})}{N} \tag{3}$$

and the variance of centroid velocity fluctuations as

$$\sigma_c^2 \equiv \frac{\sum [v_c(\boldsymbol{r}) - \mu]^2}{N}. \tag{4}$$

The *lag*, $\boldsymbol{\tau}$, and the position, $\boldsymbol{r}$, are two-dimensional vectors on the plane of the sky, and the summations in equations (1) and (2) are over the number of data pairs present at each lag, $N(\boldsymbol{\tau})$. The two-dimensional summations in equations (3) and (4) are over the face of the map, and $N = N(\boldsymbol{\tau} = \mathbf{0})$ is the total number of array elements. The centroid velocity for a discretely sampled spectral line at position $\boldsymbol{r}$ is given by

$$v_c(\boldsymbol{r}) \equiv \frac{\sum T_i(\boldsymbol{r}) u_i}{\sum T_i(\boldsymbol{r})}, \tag{5}$$

with $T_i(\boldsymbol{r})$ and u_i denoting the antenna temperature and the Doppler velocity corresponding to the ith spectrometer channel. The summation extends over the line profile.

It has been assumed in defining the ACF and SF estimators above that the data set possesses *two-point homogeneity*, which implies that the two-point probability density (and as a result, the mean and variance) is independent of position on the sky. If this were not the case, then the derived autocorrelation and structure functions would change with position in the cloud, and any conclusions drawn about the physical nature of the underlying process itself would be misleading. This homo-

geneity requirement implies that any significant large-scale gradients or trends must be filtered out of the data set prior to the statistical analysis. The filtering process we have employed is described in some detail in Appendix A.

In order for equations (1) and (2) to give meaningful results, it is also necessary to assume that the physical process giving rise to the observed centroid fluctuations is itself *ergodic*, so that ensemble averages can be approximated by spatial averages (see, e.g., Tennekes & Lumley 1972; Priestly 1981). Because ergodicity in the strictest sense requires the spatial statistics describing a process to be invariant not only across a single realization of it (i.e., a single cloud) but also across multiple independent realizations (i.e., for all the clouds in the survey), and because star formation is inherently time dependent in the sense that different regions will in all probability be at different stages in the collapse–fragmentation–star formation–cloud dispersal process, it is unlikely that the mechanism that generates the turbulence observed in molecular clouds is indeed ergodic. However, autocorrelation functions and structure functions can provide useful quantitative means for describing the flow, even if their interpretation in terms of truly ergodic, stochastic processes is somewhat uncertain.

Equations (1) and (2) represent the *unbiased* estimates for the ACF and SF, and although they do reproduce the true functions accurately near $\tau = \mathbf{0}$, they are statistically unreliable at larger lags, where the number of data pairs is small. A more robust estimate is obtained by replacing $N(\tau)$ in equations (1) and (2) with the number of data pairs at zero lag, $N(\mathbf{0})$. This *biased* estimate will always underestimate the true ACF and SF, but it is more reliable than the unbiased estimate and is therefore more useful at large lags (SF 1988b; Kleiner & Dickman 1984).

An account of the fundamental properties of the autocorrelation and structure functions can be found in SF 1988a or Townsend (1976). We will simply point out here that, with the normalization chosen, $C(\tau)$ and $S(\tau)$ are unity and zero, respectively, at $\tau = 0$ and at the largest lags, where velocities are completely uncorrelated, the autocorrelation function decays to zero while the structure function tends to the constant value 2 (if the map is truly homogeneous). It follows from equations (1) and (2) that (again, for a two-point homogeneous process) $S(\tau) = 2[1 - C(\tau)]$. If both the ACF and the SF are calculated, this relation provides a measure of how homogeneous the map actually is. However, it should be noted that there is no conclusive means for proving mathematically that a data set is indeed homogeneous, and as a result, this assumption may be a serious threat to the validity of the statistical methods presented here (Scalo 1984; SF 1988b).

All of the autocorrelation functions presented here have been calculated by first Fourier transforming the velocity centroid maps using a standard FFT routine, implemented in the Interactive Data Language (IDL), and then taking the modulus squared of that result to obtain the power spectrum. The inverse transformation of the power spectrum then yields the ACF by virtue of the autocorrelation theorem (e.g., Bracewell 1965). Note that the velocity map must be padded with zeros as discussed by Press et al. (1988) before the application of the FFT to avoid wraparound effects. The structure functions have been computed directly using equation (2).

2.2. *Error Estimation*

Before we proceed to the correlation analysis, it is important to consider how closely the biased and unbiased estimators introduced above reproduce the true autocorrelation and structure functions that characterize the underlying physical processes responsible for the observed centroid velocity fluctuations. This section is thus intended as an overview of the sources of error and the ambiguities inherent in our approach.

As mentioned above, the power spectrum is calculated as an intermediate step en route to the ACF, and for each data set, is simply given by the modulus squared of the map after applying a Fourier transformation. In actuality, this too is only an estimator and suffers from significant leakage effects when applied to a discrete data set (Press et al. 1988). However, in the present work, apart from its role in computing the ACF, we only use the power spectrum as a means for deriving certain scale properties of the turbulence in § 4.4, and since that analysis is based only on the *integral* of the spectrum, leakage should not be a problem. It should also be noted here that we have found aliasing effects (Press et al. 1988) to be negligible for all the power spectra we have computed.

Spicker & Feitzinger (1988b) have advised against the use of spectral methods in calculating the autocorrelation function, arguing that the procedure itself may introduce spurious correlations. However, we have computed the ACF directly for several of our data sets, and in all cases we find excellent agreement with the results obtained using Fourier transformations. In L1551, for example, the two methods agree to within one part in 3×10^5. We therefore conclude that any spurious effects arising from the use of spectral methods to obtain the ACF are insignificant for the data presented here.

2.2.1. *Statistical Errors and Bias*

In order to calculate the bias and statistical uncertainty of the ACF estimators precisely, it is necessary to employ an approximate model for the true ACF (Spicker & Feitzinger 1988b; Priestly 1981), which we have not attempted for the present work. This is justified because, in general, these effects are of order $1/(N)^{1/2}$, and the large number of spectra used for each analysis (see Table 1) implies that they should be negligible relative to the other errors mentioned below for all the data sets presented here, with the possible exception of regions 1a and 1b in Orion B. For a detailed account of statistical errors and bias, see Priestly (1981) and Spicker & Feitzinger (1988b).

2.2.2. *Projection Effects and Instrumental Noise*

Centroid velocity maps in an optically thin spectral line only measure radial velocities averaged along the line of sight, and any characterization of the nature of gas motions in molecular clouds is therefore inhibited by the projection smearing of the full three-dimensional velocity structure onto the plane of the sky. If the cloud depth is much larger than some characteristic length scale describing the turbulence (such as the correlation length, see below), then the observed dispersion in centroid velocities will be smaller than the true turbulent dispersion because of the statistical averaging of a large number of independent realizations of the underlying process along the line of sight (Dickman 1985; Scalo 1984). Although this underestimation is significant, Scalo (1984) finds that the observed centroid dispersion is within an order of magnitude of the true dispersion even when the cloud is much deeper than the largest turbulent length scales. The implications of this work for our results on turbulence in molecular clouds will be addressed in § 5.2.

The effect of projection smearing on the autocorrelation function itself has been studied by Kleiner & Dickman (1985), who find that it will lead to an overestimation of the actual

correlations present in the three-dimensional flow, and that the degree of the overestimation increases with the ratio of the depth of the cloud to the correlation length, λ_c, defined as the e-folding scale of the ACF (note that the correlation length discussed in this section should be viewed as an *effective* value describing the shape of the ACF, and not an absolute turbulent length scale if the velocity structure is part of a hierarchy; see § 5.2). However, the overestimation was never very severe. Even for the largest clouds they considered, with depths exceeding $10^3\lambda_c$, the apparent correlation length never exceeded the true correlation length by more than a factor of 2. Their results show further that the "observed" two-dimensional ACF preserves the essential form of the three-dimensional model functions they considered, and can therefore provide a useful measure of the true three-dimensional ACF if it is indeed isotropic (see also DK). But it should also be noted that, in a study of projection effects on the structure function, O'Dell & Castañeda (1987) find that the slope derived from the observed two-dimensional SF at lags much smaller than the depth of the cloud, is much steeper than that characterizing the true three-dimensional velocity structure (see also Kaplan & Klimshin 1964; Kaplan 1966). We will return to this matter in § 5.3.

The effect of random brightness temperature fluctuations arising from radiometer noise has been discussed in detail by Dickman & Kleiner (1985), who find that actual correlations are underestimated in the presence of instrumental noise and, in order to obtain the true, noise-free autocorrelation function, it is necessary to apply a constant multiplicative correction factor to the observed ACF at nonzero lags. We have included a brief summary of their work and of the application of their results to our observations in Appendix B. The correction factors for each data set are listed in Table 2.

2.2.3. *Beam and Sampling Effects*

The statistical approach described above can only be accomplished using a regular, evenly spaced grid of observations, and this is not always the case with an astronomical data set. For example, if triangular sampling is used or if one part of the region was mapped differently than another, then in order to apply the present analysis, it becomes necessary to interpolate the data onto a regular grid, which will to some extent influence the derived results (or, an alternative approach, which we have not considered here, is to employ the discrete correlation function described by Edelson & Krolik 1988, which was specifically designed to handle unevenly sampled data sets).[4] Furthermore, if the sampling was done at intervals less than or comparable to the beamsize, then the smoothing due to the power pattern of the antenna will introduce spurious correlations into the intensity and velocity maps. To investigate the importance of these effects for the present work, we have created several model data cubes, each composed of over 900 false spectra arranged onto a two-dimensional spatial grid. In what follows, we will describe the details of how the model velocity maps were constructed but a discussion of the primary results will be deferred to § 4.

We wish to consider first the role of beam smoothing on an otherwise random velocity field. In other words, our goal is to simulate the emission from some gaseous astronomical object for which any two adjacent measurements of an emission-line centroid velocity will be completely uncorrelated, regardless of their separation on the sky, and to construct a series of spectra by convolving that emission with the beam pattern of a radio telescope. Note that since we are dealing with spectra, the convolution must be carried out over a span of radial velocities, that is, for each spectrometer channel.

In practice, the convolution must be approximated by averaging the emission in a discrete number of pixels, or bins, weighed by the beam pattern according to their angular distance from the location on the sky where the beam is centered. With this in mind, the first step in constructing the model data cube considered in § 4 was to generate a two-dimensional array of Gaussian emission lines with a fixed strength and line width, but with a center velocity which fluctuated as a normally distributed random variable. The grid spacing was taken to be 0.1 (the units here are arbitrary, but for the sake of concreteness, we will work in arcminutes). A series of *observations* was then constructed at intervals of 1′ by calculating an average spectrum from those pixels of the original array lying within a radius of 1.7, weighed according to their distance from the beam center using the power pattern of the antenna, which was taken to be a Gaussian with a FWHM of 1.7. Thus, the number of spectra, or lines of sight, used in approximating the convolution process for each *observation* was about $\pi(1.7/0.1)^2 \approx 908$. It should be noted here that the discrete nature of the convolution implies that the models we have constructed do not actually simulate a purely random radial velocity field, but instead sample velocity structure characterized by a length scale related to the bin size of the original array, 0.1. Since a physical process generally becomes completely uncorrelated with itself beyond a few correlation lengths, this implies that the objects we have simulated in our models have velocity correlation lengths of about 0.05 or less, which is more than 30 times smaller than the FWHM of the beam.

After the model data cube was constructed, the artificial spectra were subjected to the same analysis applied to the actual observations (see § 3.2). In particular, the model data was interpolated onto a square grid with spacing 0.5 (half that of the sample spacing used for the observations themselves), and a centroid velocity map was computed. The interpolation scheme used in constructing velocity maps both for the model spectra and for the actual observations is what we will refer to as *cone interpolation*. This simply means that the centroid velocity at a particular point in the sky is calculated by first interpolating the data from all nearby observations to obtain a spectrum at the desired location, and then applying equation (5). Each individual observation used to compute the interpolated spectrum is weighed according to the formulae:

$$W \propto 1 - \frac{r}{r_0} \qquad r < r_o$$

$$= 0 \qquad r \geq r_o$$

where W is the appropriate weight, r is the angular distance between the observation and the point on the sky for which the spectrum is being computed, and r_o is the interpolation radius. The interpolation radius for the model data (and for most of the observational data, see § 3.2) was chosen to be 1.1. The model results are shown in Figures 4, 7, and 9, and discussed in §§ 4 and 5.

Several additional models were computed in a similar manner for different sampling grids and interpolation radii.

[4] The authors would like to thank J. M. Shull for bringing this work to their attention.

We find that the statistical properties of oversampled and critically sampled velocity maps are virtually identical for the models, and thus conclude that the effects of grid spacing are minimal (within certain limits). This conclusion was verified in a similar investigation of sampling effects using the L1228 data. In contrast, the interpolation process was found to have a noticeable influence on the autocorrelation and structure functions. These effects were investigated for the model data cubes and for the L1228 and HH 83 observations, and it was found that increasing the interpolation radius tended to shift the entire ACF up slightly, preserving its general form, but introducing small spurious correlations. In addition, the shift was more pronounced for very small lags, so that the innermost points on the azimuthally averaged ACFs and SFs presented in Figures 2, 3, 5, and 6 are probably influenced by the interpolation process and should be excluded from the curve fits (see § 4). However, if the interpolation radius was not too large, although these effects were noticeable, they were not appreciable, and our conclusions about the nature of turbulence in the objects studied remain unaltered. In particular, for the interpolation radii used in the observations presented here, we find that the spurious effects arising from the interpolation process lead to an overestimate of the correlation length, λ_c, of no more than 10% and have only a minor influence on the overall shape of the statistical functions and on the results presented in § 4.

3. OBSERVATIONS

3.1. *Data*

This paper presents the first results of a massive multiyear effort to survey the structure and kinematics of nearby molecular clouds. Over the course of 5 years, over 10^6 spectra were obtained with the AT&T Bell Laboratories 7 m offset Cassegrain antenna, located in Holmdel, New Jersey. This paper is based on a 300,000 spectrum subset of this molecular cloud survey database that uses observations of the 110 GHz $J = 1$–0 ^{13}CO, 109 GHz $C^{18}O$, and the 98 GHz $J = 2$–1 CS line. The 7 m telescope has a very clean Gaussian beam with a FWHM of 100″ between 98 and 115 GHz with a primary beam efficiency of about 87% and an aperture efficiency of about 55% that is determined by the 14 dB edge taper of the illumination pattern.

Observations used in this paper were obtained between 1985 December and 1991 June. During the beginning of this period, we used liquid helium-cooled SIS receivers built at AT&T Bell Laboratories that used Pb junctions produced by Ron Miller. These Pb junction receivers had system temperatures ranging from $T_{SSB} \sim 60$–250 K but suffered degradation with time and repeated thermal cycling and required frequent replacement. In 1989 we switched to a mixer-block built by NRAO that used more stable Nb junctions with a single sideband temperature $T_{SSB} \sim 75$–130 K.

The 7 m antenna is equipped with a flexible spectrometer system consisting of 512 channels of 1 MHz wide filters (consisting of two 256 channel filter-banks), and a 256 channel filter bank consisting of 0.25 MHz wide filters. The 0.25 MHz filter bank can be split into two 128 channel halves. The IF processing electronics include a spectrum expander (Henry 1976) that can send a copy of the IF signal to one 128 channel half of the 0.25 MHz spectrometer to produce a variable effective channel bandwidth (resolution) of 100, 50, 25, or 12.5 kHz per channel. A given spectral feature can be observed simultaneously with 512 channels of 1 MHz filters, 128 channels of 0.25 MHz filters, and 128 channels of 0.25 MHz filters that have been processed through the spectrum expander to provide higher resolution. Most of the data used in this paper were taken with the 100 kHz resolution option of the spectrum expander which gives a velocity resolution of 0.26 km s^{-1} at 115 GHz.

The observations were made by both in-band frequency switching, in which the reference frequency is displaced from the signal by 6.4 MHz, as well as the multiple-mapping position-switching mode described by Bally et al. (1987). All data were calibrated with a blade chopper that permits rapid comparison between the sky and a 77 K liquid nitrogen–cooled reference load or the 77 K load and an ambient temperature absorber. The receiver noise temperature and the temperature scale are determined by comparing a room temperature load to the liquid nitrogen load. Then the sky brightness temperature is measured by comparison of the sky emission with the cold load. A simple atmospheric model is used to scale the observed intensities to the brightness temperature that would have been measured by this antenna above the atmosphere. The details of the receiver and calibration procedure have been described elsewhere (Pound, Bania, & Wilson 1990).

During the course of data acquisition the Bell Labs group developed semiautomated schedule-driven observing that permitted the 7 m antenna to conduct a sequence of observations at a given frequency for up to 48 hr without the presence of an operator. The key ingredient of this automated observing is a macro-driven observing control program, OBS (to be described elsewhere), that features automated integration time estimation. SKY scans (spectra obtained by switching between blank sky and a 77 K load) are used to determine the sky brightness temperature and opacity. The resulting estimate of the system temperature and the source elevation are used to calculate the observing time required to obtain a spectrum that has a specified noise level at a specific resolution. The scheduler is triggered to shift sources according to the control macro prescription at either a scheduled time, or when a source sets to a prescribed elevation. An infinite loop can be used to sequence observations that continue for an indefinite period of time, which in practice is limited to 48 hr by cryogen replenishment requirements.

The L1228, L1551, Mon R2, and Orion B observations are all part of the Bell Labs survey, but in order to cover a larger range in scales with the present analysis, we have included an additional data set spanning a region just west of L1641 in the Orion A cloud that was obtained with a higher spatial resolution (beamwidth = 0.′22) using the IRAM 30 m telescope on Pico Veleta, Spain in 1989 April and December. For a more detailed discussion of these observations, see Bally et al. (1994).

All data were reduced using the COMB spectral line reduction package. Frequency-switched spectra were folded, and linear baselines were removed from the spectra. Baselines were fitted to that portion of the spectrum that is devoid of emission. After inspection of the maps and images, additional problems, such as bad channels, were fixed. COMB was used to generate sets of spatial-spatial and spatial-velocity contour maps and FITS images. The COMB program features an automated "data extraction" and reduction package that searches the raw data archived for spectra that satisfy certain requirements such as location within a window of interest on the sky and in frequency space, and have the desired back-end configuration and noise requirements. The map-extraction

TABLE 1

OBSERVED CLOUDS

NAME	TRANSITION	CENTER COORDINATES α(1950)	CENTER COORDINATES δ(1950)	NUMBER OF SPECTRA	HALF-POWER BEAMWIDTH	VELOCITY RESOLUTION (km s^{-1})
HH 83	^{13}CO $J = 2 \rightarrow 1$	05^{h}31^{m}06^s.3	−06°31′45″	1558	0.′22	0.13
L1228	^{13}CO $J = 1 \rightarrow 0$	20 58 00.0	+77 23 00	883	1.7	0.27
L1551	^{13}CO $J = 1 \rightarrow 0$	04 28 40.0	+18 01 42	1181	1.7	0.14
Mon R2:						
1	^{13}CO $J = 1 \rightarrow 0$	06 05 22.0	−06 22 25	2157	1.7	0.27
2				1949	1.7	0.27
3				3052	1.7	0.27
Orion B:						
1a	^{13}CO $J = 1 \rightarrow 0$	05 41 08.1	−01 05 00	205	1.7	0.27
1b				523	1.7	0.27
1c				1200	1.7	0.27
2				4605	1.7	0.27
3				5216	1.7	0.27
4				5469	1.7	0.27

routines execute a prespecified set of reduction instructions, placing the spectra into reduced data files and automatically producing FITS data cubes ready for inspection.

Integrated intensity contour maps for the HH 83 molecular cloud, L1228, L1551, Mon R2, and Orion B are presented in Figure 1. Each data set is labeled with the appropriate transition (^{13}CO $J = 2 \rightarrow 1$ for the HH 83 data and ^{13}CO $J = 1 \rightarrow 0$ for the others) and the LSR velocity range over which the intensity was integrated (in km s^{-1}). The center coordinates, the number of spectra, the half-power beamwidth, and the velocity resolution for each region are listed in Table 1. Several of the clouds surveyed, in particular Mon R2 and Orion B, were clearly composed of several distinct approximately Gaussian velocity components that were isolated in space and velocity prior to the statistical analysis, which was then applied to each region separately. To facilitate the extraction of the different Gaussian components, we have introduced convenient relative coordinate systems for L1551 and Orion B, and the relationship of these coordinates to right ascension and declination is shown by a directional indicator on each map in Figure 1. In Orion B, many of the distinct components overlapped, and it was not possible to isolate them spatially. For these regions, it was necessary to separate the components in velocity by performing the summation in equation (5) over carefully selected velocity ranges, chosen by considering the mean spectra, and then to combine the data from neighboring regions to obtain a map of the entire component. For example, region 3 in Orion B almost certainly lies in front of regions 2 and 4, and in order to isolate it, several subregions (see Fig. 1*e*) were integrated over the lsr velocity ranges [3.0, 9.2] km s^{-1} (region 3a) and [1.0, 7.5] km s^{-1} (region 3b), and then juxtaposed to obtain region 3. The higher velocity components ([9.2, 11.9] km s^{-1} and [7.5, 12.7] km s^{-1}) are defined as regions 2b (which was juxtaposed with the nonoverlapping area, region 2a, in a similar manner to obtain region 2), and region 4 respectively.

3.2. *Constructing the Velocity Maps*

Velocity centroid maps were constructed for each of the 12 regions defined above by interpolating the observed spectra onto an oversampled, regular grid using the cone interpolation scheme described in § 2.2.3. The grid spacing and interpolation radius used for the Orion B, Mon R2, L1228, and L1551 data were chosen to be 0.′5 and 1.′1 respectively, while those used for the HH 83 molecular cloud observations were 0.′05 and 0.′25. All lines of sight for which the average integrated intensity was below a threshold level were ignored in the analysis. The threshold levels, in K km s^{-1}, were as follows: 2.5 for Orion B and Mon R2, region 1; 2.0 for regions 2 and 3 in Mon R2; 1.5 for L1228 and L1551; and 1.0 for HH 83. In order to further suppress spurious emission that was not associated with the clouds themselves, it was in some cases necessary to impose a further restriction on which lines of sight to include in the analysis, and for these a threshold temperature was introduced, and all grid points for which the associated peak brightness temperature fell below the threshold were replaced with null pixels. The velocity windows, where possible, were chosen to span about $12\sigma_p$ (σ_p is the *parent* dispersion defined in § 4.1) and were centered on the mean velocity of the ensemble mean spectrum. A larger velocity range is not recommended because the influence of noise is very sensitive to the number of channels used to calculate the centroid (DK 1985). In some cases it was necessary to integrate over a smaller window in order to isolate particular Gaussian components (see above).

4. RESULTS

4.1. *Fluctuation Amplitudes*

Correlation functions provide important insight into the scale properties of a turbulent flow, but in order to understand fully the role that turbulence plays in the dynamics of molecular clouds, it is also necessary to consider the mean amplitude of the gas motions. Three fundamental statistical measures intended to characterize the observed velocity fluctuation amplitudes have been introduced by Dickman & Kleiner (1985). The first, which they call the *parent* dispersion σ_p, is the root mean square of the radial velocity fluctuations averaged over the entire volume of the cloud and, for an optically thin line, can be obtained by combining all the observations in the region and fitting a Gaussian to the ensemble mean spectrum (note that *fluctuations* here merely means that the mean velocity μ has been subtracted out, so σ_p in general will include contributions from both systematic and turbulent motions; see eq. [8]). The second is a measure of the typical spread in the

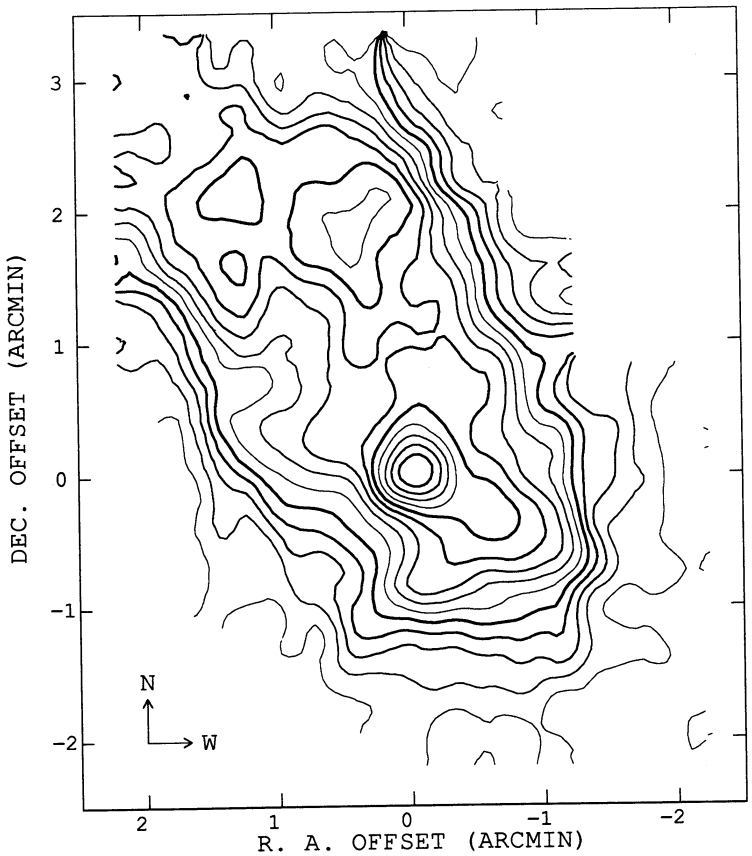

FIG. 1*a*

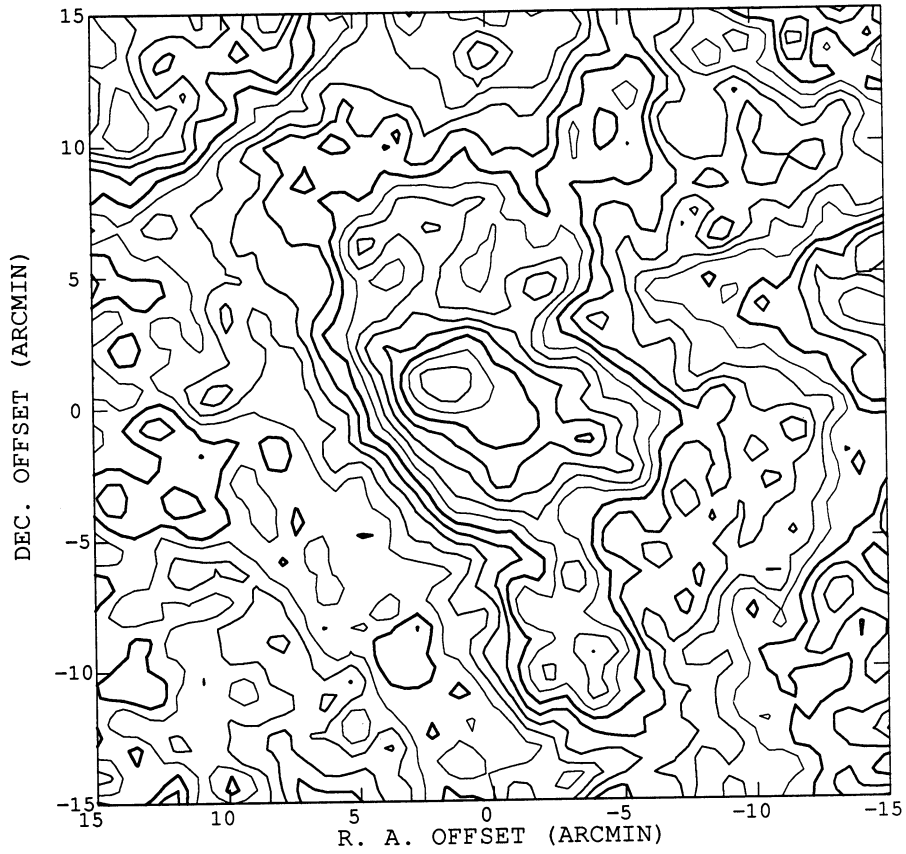

FIG. 1*b*

FIG. 1.—Integrated intensity maps of ^{13}CO emission for each of the five molecular clouds surveyed. The HH 83 data were taken in the $J = 2 \rightarrow 1$ transition, and the rest in the lowest rotational level, $J = 1 \rightarrow 0$. The center coordinates for each region are listed in Table 1, and the directional indicators on each plot show the relationship between the adopted coordinate system and the right ascension/declination standard. The contour levels (in K km s^{-1}) for HH 83, L1228, and L1551 (panels *a*, *b*, and *c*) are from 0.5 to 8.5 in steps of 0.5, and for Mon R2 and Orion B (panels *d* and *e*) they are from 4.0 to 48.0 in steps of 4.0. The lsr velocity integration ranges (in km s^{-1}) are as follows: (*a*) HH 83: [5.0, 7.5], (*b*) L1228: −10.0, −5.0], (*c*) L1551: [5.5, 8.1], (*d*) Mon R2: [5.0, 18.0], and (*e*) Orion B: [1.0, 15.0].

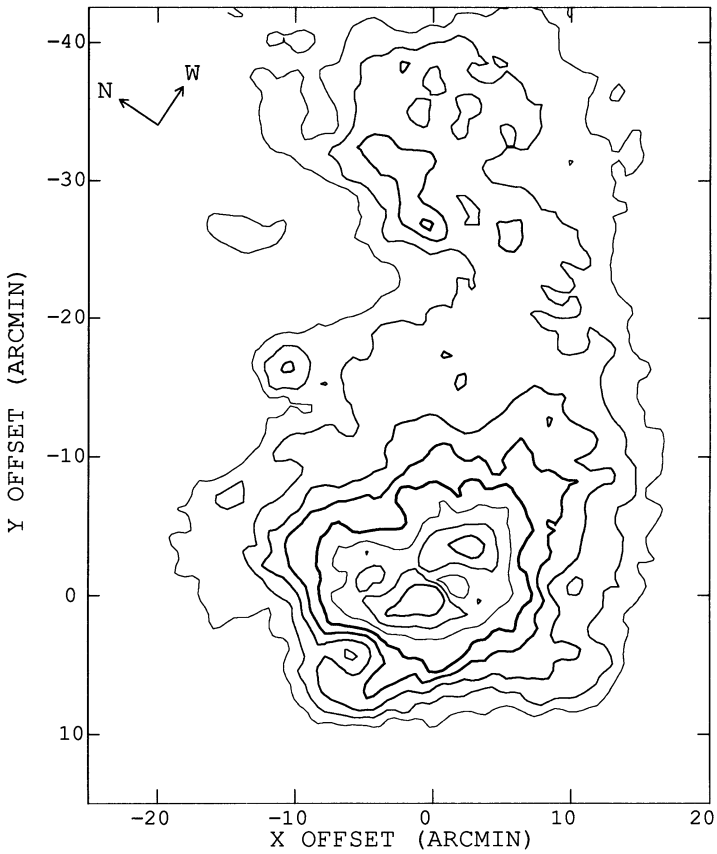

FIG. 1*c*

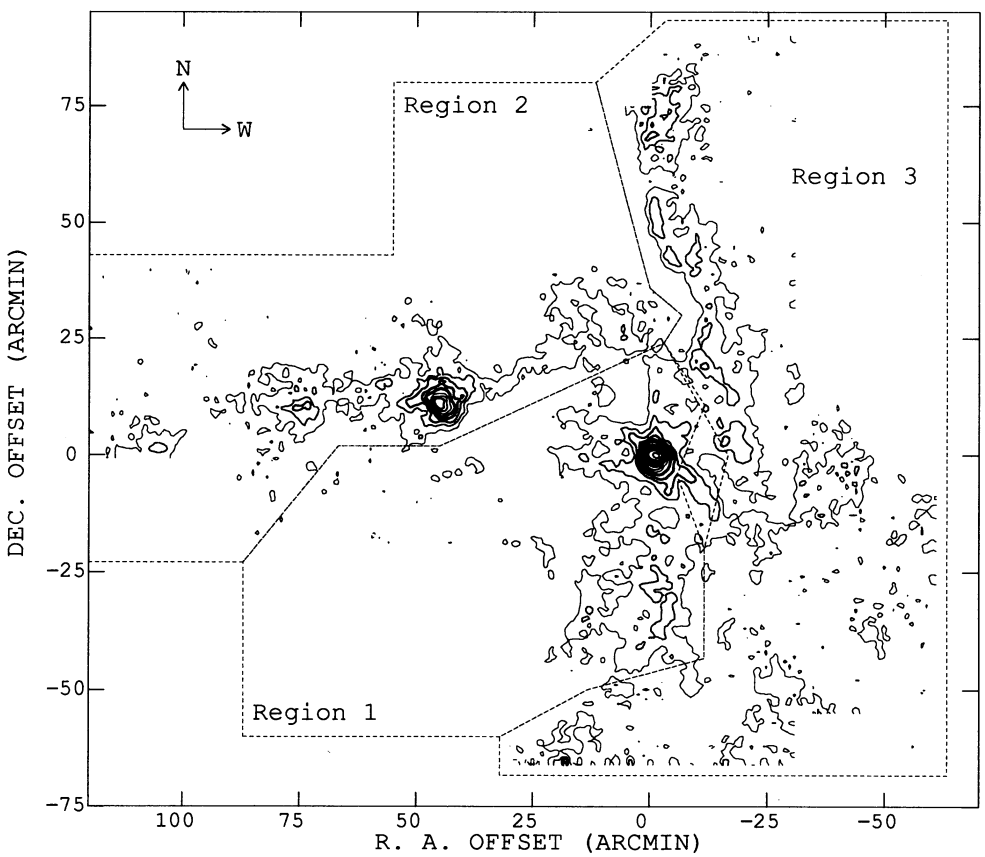

FIG. 1*d*

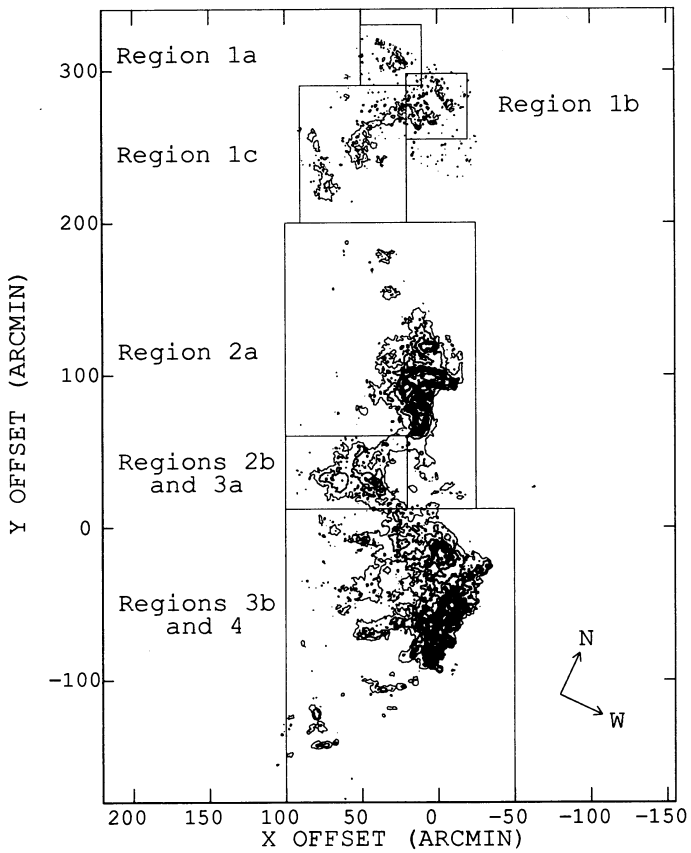

FIG. 1*e*

radial component of gas motions along each line of sight. This is the internal dispersion, σ_i, discussed in Appendix B, and is simply an average line width for the region. The third statistical measure is the centroid velocity dispersion, σ_c, given by equation (4). As discussed in Appendix B, the observed centroid dispersion includes a contribution due solely to instrumental noise that must be removed to obtain the *true*, or noise-free, dispersion, σ_c^*. From equation (B1), $\sigma_c^* = (\sigma_c^2 - \sigma_n^2)^{1/2}$, where σ_n^2 is the noise variance defined in Appendix B. For an optically thin line, the parent, internal, and noise-free centroid dispersions are related (DK 1985):

$$\sigma_p^2 = (\sigma_c^*)^2 + \sigma_i^2 \ . \qquad (6)$$

In order to employ this expression as a check on the consis-

TABLE 2

STATISTICAL MEASURES[a]

Region	Mean Signal/ Noise (S/N)	Mean LSR Velocity (μ)	Observed Centroid Dispersion (σ_c)	Noise-free Centroid Dispersion (σ_c^*)	ACF Noise Correction [$C^*(\tau)/C(\tau)$]	Internal Dispersion (σ_i)	Indirect Parent Dispersion (σ_p')	Parent Dispersion (σ_p)	Turbulent Centroid Dispersion (σ_{ct}^*)	Turbulent Dispersion (σ_t)
HH 83	19.7	6.19	0.23	0.23	1.01	0.38	0.44	0.42	0.12	0.39
L1228	5.9	−7.59	0.39	0.38	1.08	0.55	0.67	0.74	0.08	0.64
L1551	8.4	6.90	0.34	0.34	1.04	0.36	0.49	0.50	0.16	0.43
Mon R2:										
1	8.8	10.01	0.61	0.60	1.04	0.67	0.90	1.12	0.35	1.03
2	6.3	12.02	0.41	0.40	1.04	0.62	0.84	0.74	0.21	0.67
3	5.8	12.59	0.47	0.46	1.04	0.75	0.88	0.83	0.28	0.76
Orion B:										
1a	6.4	10.60	0.16	0.14	1.22	0.53	0.55	0.55	0.13	0.54
1b	6.4	9.04	0.29	0.27	1.12	0.57	0.63	0.55	0.20	0.53
1c	5.4	10.43	0.57	0.54	1.09	0.60	0.81	0.83	0.32	0.76
2	8.8	9.80	0.81	0.77	1.11	0.65	1.00	1.15	0.23	0.91
3	4.6	5.19	1.41	1.39	1.02	1.45	2.01	2.05	0.60	1.66
4	8.7	9.96	0.77	0.76	1.02	0.80	1.10	1.31	0.45	1.17
Heiles Cloud										
2[b]	...	5.96	0.30	0.29	1.09	0.68	0.74	0.77	0.21	0.74

[a] All quantities, with the exception of S/N and the ACF noise correction, are given in km s^{-1}.
[b] Kleiner & Dickman 1987.

tency of our results, we define a new variable, the indirect approximation of the parent dispersion, as $\sigma_p' \equiv (\sigma_c^{*2} + \sigma_i^2)^{1/2}$. The statistical measures described here are exhibited in Table 2 for our observations and for a similar study of Heiles cloud 2 in the Taurus dark cloud complex by Kleiner & Dickman (1987). Also shown are the average signal-to-noise ratio (S/N), the mean centroid velocity in the lsr frame, μ, and the ACF noise correction, $C^*(\tau)/C(\tau)$ (see eq. [B2]), for each region. Denoting the peak brightness temperature at position $\boldsymbol{r}$ as $T_{\max}(\boldsymbol{r})$ and the rms amplitude of noise-induced fluctuations at $\boldsymbol{r}$ as $\delta T(\boldsymbol{r})$, we define the average signal-to-noise ratio to be

$$S/N \equiv \langle T_{\max}(\boldsymbol{r})\rangle / \langle \delta T(\boldsymbol{r})\rangle \ . \tag{7}$$

The angular brackets represent spatial averages over the face of the cloud. Also shown in Table 2 is the centroid dispersion due solely to the fluctuating, or turbulent, velocity component, σ_{ct}^*. This is obtained from the residual centroid maps after the systematic velocity component has been removed as described in Appendix A. The asterisk indicates that the noise variance has been subtracted (in quadrature, as with σ_c^*). The final entry in the table is the total amplitude of turbulent velocity fluctuations averaged over the volume of the cloud, σ_t. If the contributions of the systematic and noise components to the parent dispersion are independent of one another and of the turbulent, or fluctuating, component, then

$$\sigma_t \equiv \sqrt{\sigma_p^2 - \sigma_{cs}^2 - \sigma_n^2} \ , \tag{8}$$

where σ_{cs} is the dispersion of the smoothed centroid velocity map (Appendix A). If the systematic and fluctuating velocity components were truly independent, then σ_c^2 would be equal to $\sigma_{cs}^2 + (\sigma_{ct}^*)^2 + \sigma_n^2$. In practice, we found this decomposition to be only approximately valid.

A few features of Table 2 should be noted before we proceed. First, the turbulent velocity disperion, σ_t, is never much less than the parent dispersion, σ_p, implying that the turbulent component of gas motions contributes a significant amount to the bulk kinetic energy budget of the cloud. Also, the direct estimate for the parent dispersion, σ_p, agrees with the indirect

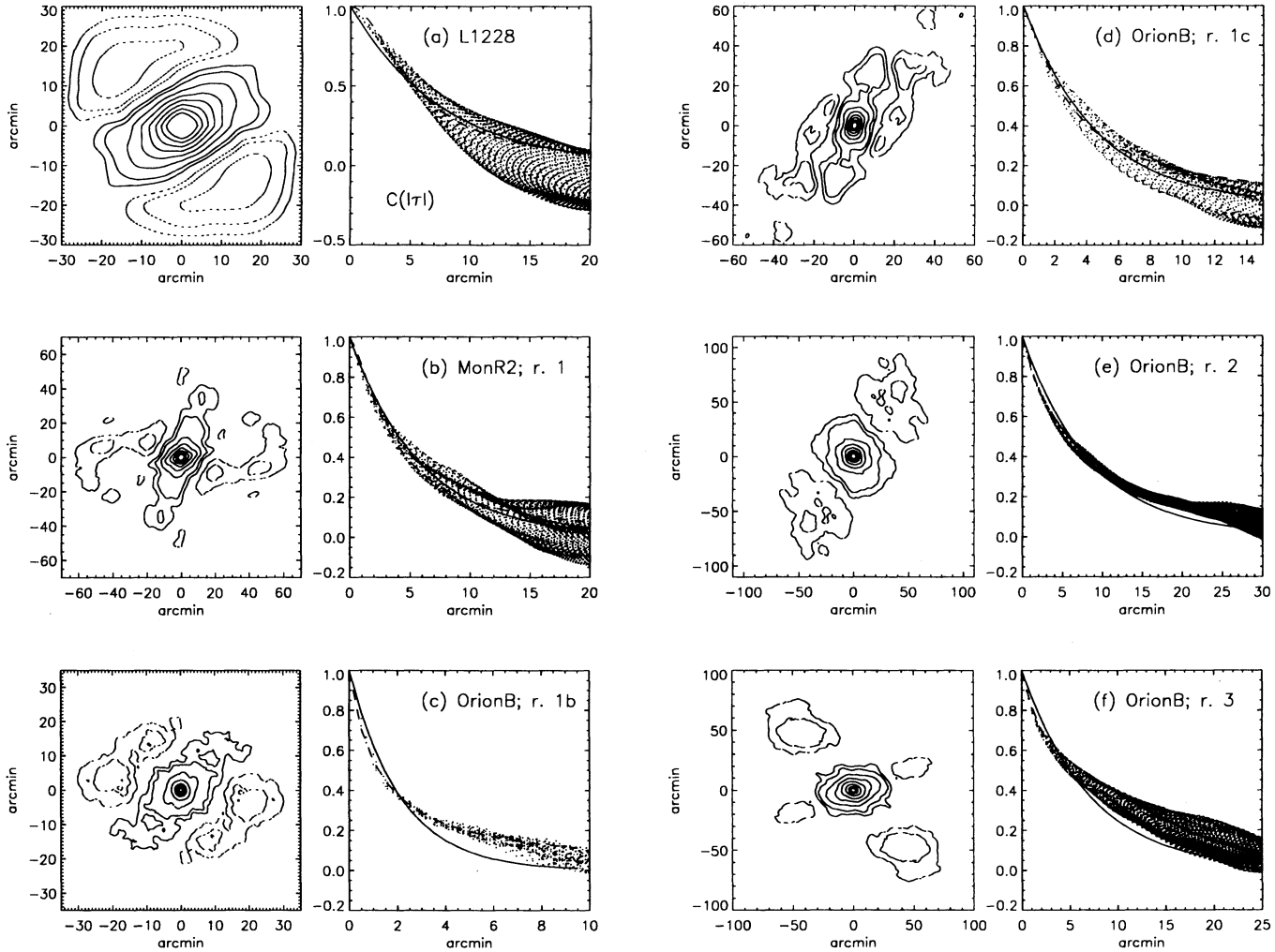

FIG. 2.—Shown are several illustrative examples of the biased autocorrelation functions for the raw (unfiltered) data. The various regions are defined in § 3.1. Each panel (*a*) through (*f*) includes a contour plot of the two-dimensional ACF and a scatter plot of the array values (*dots*) as a function of the magnitude of their corresponding vector lag, $|\tau|$. The solid and dashed lines indicate the best fit of the azimuthally averaged ACF to an exponential ($e^{|\tau|/\tau_e}$) and a power-law $\{1/[1 + (|\tau|/\tau_o)^n]\}$ form. The parameters τ_e, τ_o, and n are given in Table 3 for each region. The contour levels are −0.5, −0.4, −0.3, −0.2, −0.1, −0.05, 0.05, 0.1, 0.2, 0.3, 0.4, 0.5, 0.6, and 0.7, and anticorrelations are denoted by dotted lines. All lags are given in arcminutes.

estimate, σ'_p to within 20% in all cases, verifying the consistency of our results. Any discrepancy can probably be attributed to the uncertainty in determining σ_i and σ_n discussed in Appendix B.

4.2. *Autocorrelation Function*

Several illustrative examples of the biased autocorrelation functions for the raw data are exhibited in Figure 2. The unbiased estimators are similar and have been omitted from the presentation to save space. Each of these figures, panels (*a*) through (*f*), includes a contour map of the two-dimensional ACF and a scatter plot of the actual ACF array values as a function of the magnitude of their corresponding lag, $|\tau|$. The reflection symmetry of the ACF, evident in the contour maps, follows directly from its definition in equation (1). Many of the unfiltered maps exhibit a significant large-scale, systematic component that manifests itself in the autocorrelation function as anticorrelations for lags in the direction (or opposite the direction) of the gradient and positive correlations for lags perpendicular to it. This property of the ACF was exploited by Spicker & Feitzinger (1988a) to obtain a value for the mean direction of the kinematical major axis of the LMC. Large-scale gradients are most evident in the L1228 map of Figure 2*a*, and in the HH 83 and L1551 data, which look similar and are therefore not shown. Note also the anticorrelations in all four directions from an approximately isotropic central region in the contour map for the Orion B, region 3, data. The results for the remaining regions not shown in Figure 2 resemble closely those that are presented. Similar plots calculated using the filtered data are exhibited in Figure 3 for all 12 regions we have surveyed.

It is apparent from the contour and scatter plots that the ACFs are approximately circularly symmetric at small lags, and it is therefore reasonable to consider the average of the autocorrelation functions over azimuthal angle in deriving scale properties of the velocity fluctuations and to compare their characteristics to theoretical models of homogeneous, isotropic, turbulent flows. In particular, the circular symmetry implies that the velocity structure can be approximately characterized by a single correlation length, λ_c, which is simply the *e*-folding distance of a one-dimensional slice through the two-dimensional ACF. The spread of points in the scatter plots is a measure of how isotropic the two-dimensional ACFs actually are, and any departure from isotropy will give a range of possible values for λ_c. The observed correlation lengths, and the

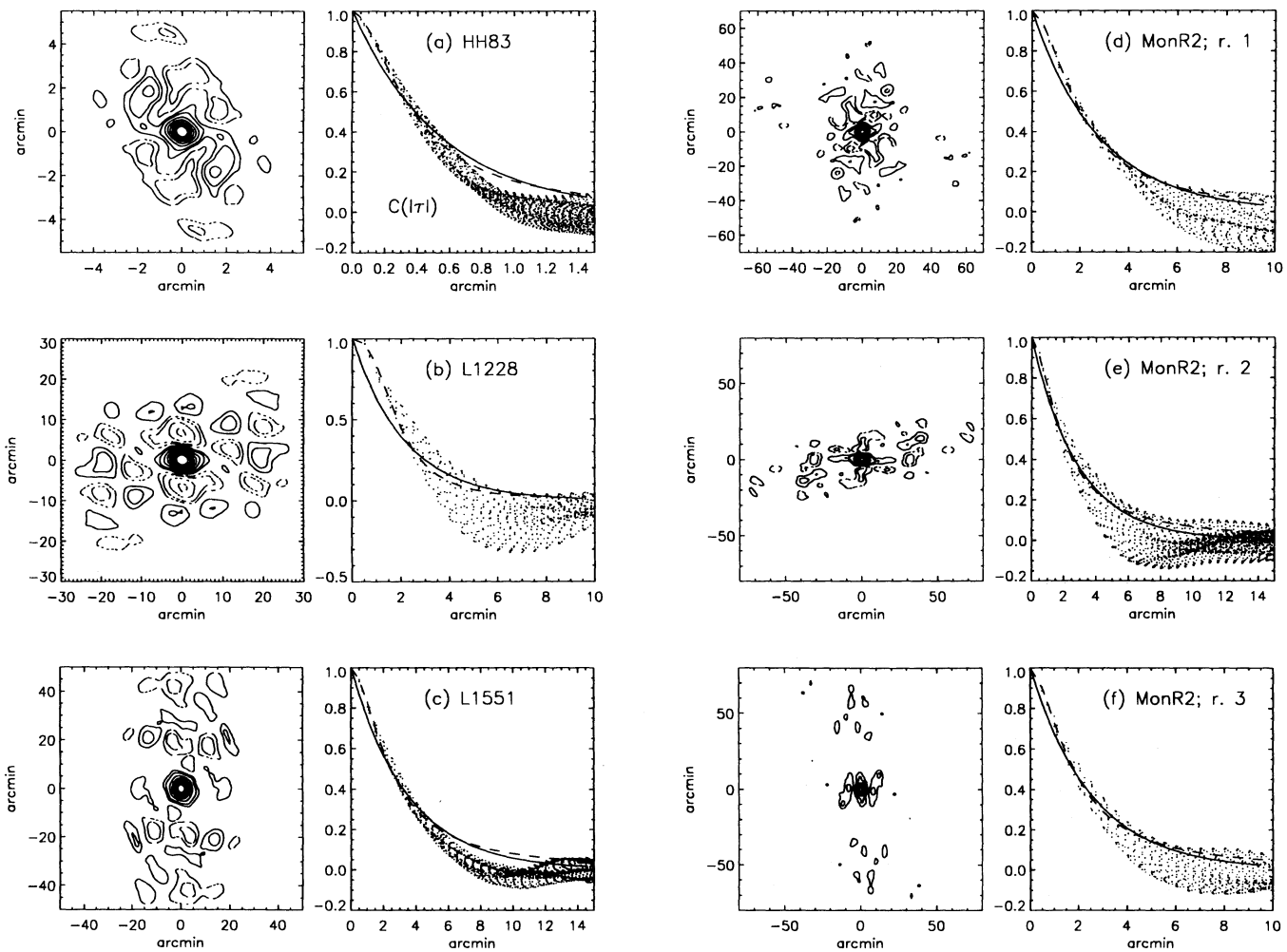

FIG. 3.—Similar to Fig. 2, but for the filtered data, and including all of the clouds in our survey. These ACFs have been corrected for instrumental noise using eq. (B2).

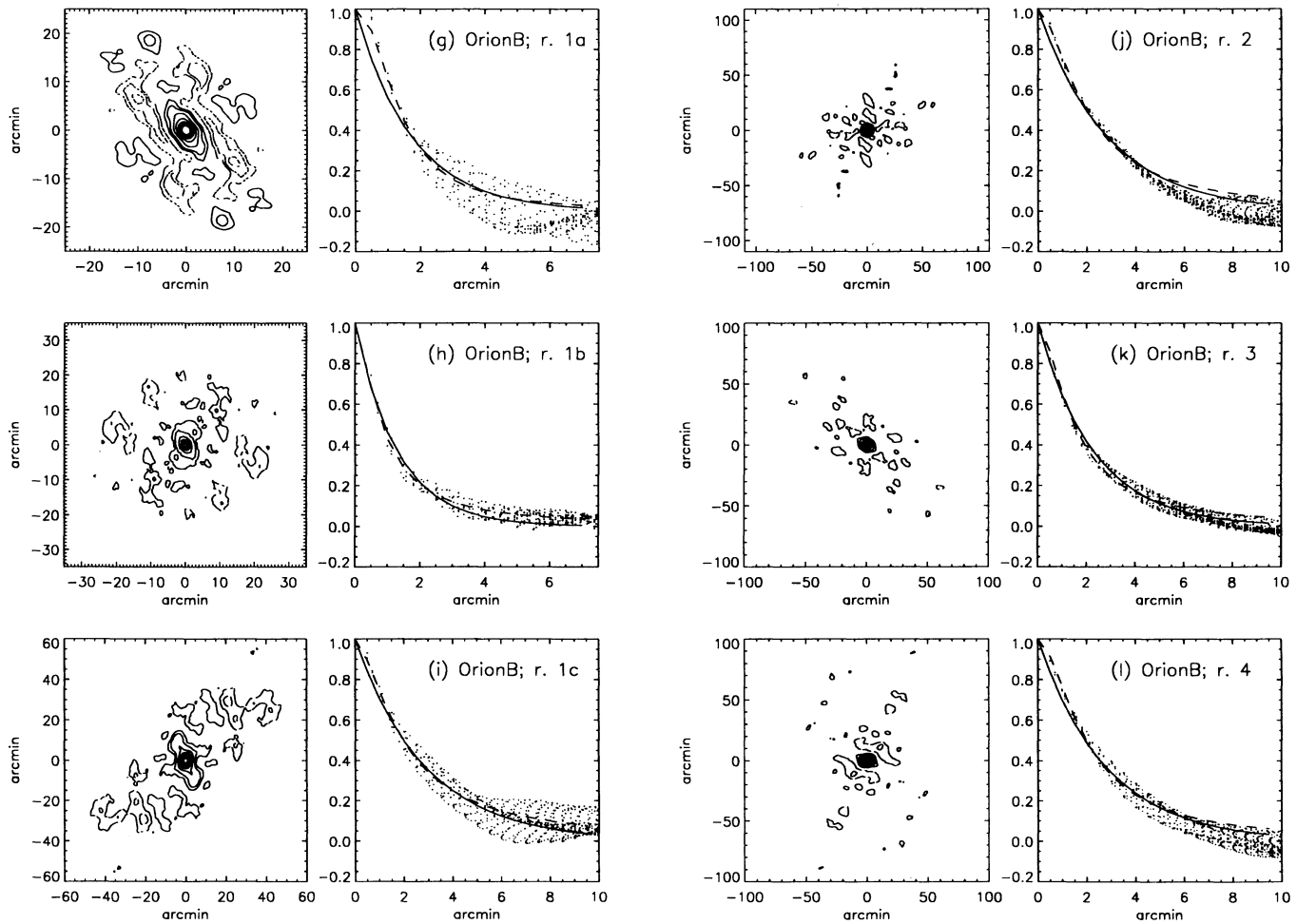

FIG. 3—*Continued*

range of their directional variation, derived from both the biased and unbiased ACF estimators are exhibited in Table 3 for the raw centroid velocity data and for the residual (filtered) maps. All of the results listed in Table 3 and presented in Figure 3 for the filtered maps have been corrected for instrumental noise as described in Appendix B.

We have also fitted the azimuthally averaged ACF, $C(|\tau|)$, to the functional forms introduced by Scalo (1984), $\exp(-|\tau|/\tau_e)$ and $1/[1+(|\tau|/\tau_o)^n]$, and have superposed the best-fit results on the scatter plots of Figures 2 and 3 (solid lines denote the exponential forms and dashed lines the power-law forms). Table 3 lists the parameters, τ_e, τ_o, and n, for each of the curves along with the analogous results obtained from the unbiased ACF estimators. Note that in general the ACFs of Figure 2 are characterized by a sharp dropoff at small lags, followed by a more gradual decrease on scales larger than the correlation length, which cannot be modeled accurately with a simple exponential form. Kleiner & Dickman (1987) have interpreted this behavior as indicating shear layer turbulence in Heiles Cloud 2 in Taurus. However, it could also be attributed to the effects of large-scale gradients (notice that the filtered results of Figure 3 tend to decay *more* rapidly than the exponential fits for large lags) or to increased correlations at small lags due to beam smoothing (see § 5.1).

Notice that the calculated ACFs were not in general described very well by either the power-law or the exponential models, but the former did, on average, give slightly better fits (possibly only because the power-law fits include two free parameters). However, both types of fits, and in particular the best-fit values for the exponent, n, were found to be sensitive to the precise value of the ACF near $|\tau| = 0$, where beam smoothing (enhanced slightly by the interpolation procedure; see § 2.2.3) dominates, and where the noise correction (which is somewhat uncertain for the more complicated regions; see Appendix B) plays an important role. For these reasons, the fit parameters τ_e, τ_o, and n listed in Table 3 should only be regarded as approximate descriptions of the true azimuthally averaged ACF. Similar results for the model data cube discussed in § 2.2.3 are shown in Figure 4 and listed in Table 3.

4.3. *Structure Function*

Departures from stationarity due to large-scale systematic motions will contaminate the small-scale structure of the ACF and will therefore inhibit any autocorrelation analysis of turbulent velocity fluctuations. In contrast, the structure function is less sensitive to systematic trends and can still characterize small-scale fluctuations even in the presence of linear gradients (Scalo 1984; Townsend 1976). For this reason, we have computed the SF in addition to the ACF, and our results are exhibited in Figures 5 and 6 for both the raw and the filtered

TABLE 3

TURBULENT LENGTH SCALES[a] AND SCALING LAWS

		Unfiltered Data				Filtered Data			
Region	Estimator	Correlation (e^{-1}) Length [λ_c(range)][b]	Exponential Scale (τ_e)	Power-Law Scale (τ_o)	Power-Law Exponent (n)	Correlation (e^{-1}) Length [λ_c(range)][b]	Exponential Scale (τ_e)	Power-Law Scale (τ_o)	Power-Law Exponent (n)
HH 83	Biased	0.95(±0.15)	1.0	0.69	1.5	0.51(±0.06)	0.57	0.38	1.7
	Unbiased	1.55(±0.5)	1.6	1.0	1.6	0.58(±0.08)	0.72	0.45	1.8
L1228	Biased	7.5(±1.8)	7.5	5.3	1.8	2.8(±0.5)	2.2	1.9	2.6
	Unbiased	13.0(±5.5)	11.6	7.4	1.8	3.0(±0.5)	2.4	2.0	2.7
L1551	Biased	8.0(±1.3)	7.6	4.9	1.5	3.6(±0.4)	3.5	2.5	1.7
	Unbiased	14.5(±6.0)	12.4	8.3	1.3	4.0(±0.4)	4.3	2.9	1.8
Mon R2:									
1	Biased	5.9(±1.3)	5.9	3.5	1.4	2.7(±0.2)	2.8	2.0	1.8
	Unbiased	8.5(±1.5)	9.4	6.3	1.5	3.4(±0.2)	3.8	2.6	2.0
2	Biased	6.5(±2.0)	6.0	3.8	1.2	2.9(±0.6)	2.9	2.0	1.6
	Unbiased	15.0(±5.0)	10.5	7.2	1.3	3.8(±0.8)	4.0	2.6	1.8
3	Biased	4.2(±0.7)	4.0	2.6	1.3	2.6(±0.4)	2.5	1.8	1.7
	Unbiased	8.2(±2.3)	7.9	5.3	1.3	3.6(±0.4)	3.6	2.5	2.0
Orion B:									
1a	Biased	1.7(±0.3)	1.7	1.2	1.7	1.7(±0.3)	1.7	1.4	2.1
	Unbiased	2.8(±0.8)	2.5	1.8	1.8	2.8(±0.8)	2.6	1.9	2.4
1b	Biased	2.1(±0.05)	2.1	1.2	1.0	1.2(±0.2)	1.3	0.83	1.6
	Unbiased	5.5(±2.0)	3.1	2.1	0.82	1.5(±0.3)	1.6	1.0	1.4
1c	Biased	4.6(±0.6)	4.6	3.0	1.3	3.0(±0.5)	2.9	2.0	1.6
	Unbiased	8.5(±3.0)	10.1	6.3	1.6	4.5(±1.3)	4.7	3.2	1.8
2	Biased	9.0(±1.0)	8.6	5.2	1.1	3.0(±0.3)	2.8	2.0	1.7
	Unbiased	18(±5.0)	15.3	10.9	1.1	3.5(±0.3)	3.6	2.5	1.7
3	Biased	9.5(±1.5)	7.1	4.9	0.98	2.2(±0.3)	2.3	1.5	1.7
	Unbiased[c]	...	...	...	...	3.9(±0.6)	3.6	2.5	1.7
4	Biased	7.3(±1.3)	7.4	4.3	1.1	3.0(±0.5)	2.8	2.0	1.7
	Unbiased	17.5(±5.0)	13.2	9.3	1.1	3.6(±0.6)	3.6	2.6	1.8
Model	Biased	1.5(±0.05)	1.3	1.2	3.0	...	...	...	...
	Unbiased	1.6(±0.05)	1.4	1.3	3.0	...	...	...	...

[a] All distances are given in arcminutes.

[b] The range given is that arising from the anisotropy of the ACFs (see § 4.2).

[c] For Orion B, region 3, the number of nonzero pixels, $N(\tau)$, decreases more rapidly with lag than the biased ACF, so the unbiased ACF exceeds unity at some lags and is therefore unphysical (see eq. [7]).

data. Shown are one-dimensional scatter plots, similar to those in Figures 2 and 3, of the array values comprising the two-dimensional structure function for each region. The filtered maps (Fig. 6) have been corrected for intrumental noise using equation (B3). We have calculated only the unbiased versions of the SF because in what follows, we are primarily concerned with the functional form of the structure function at small lags, where the number of data pairs, $N(\tau)$, is large and where the statistical error of the unbiased estimator is therefore not a problem. Notice that most of the filtered maps tend to the constant value two at large lags, suggesting that they are indeed homogeneous, at least in terms of the variance (§ 2.1).

Phenomenological results in the theory of forced isotropic turbulence predict cascade processes (in some situations) where quantities such as the structure function take on power-law forms, that is, $S(|\tau|) \propto |\tau|^s$, within a range of scales (or wavenumbers) known as the inertial subrange (see §§ 4.4, 5.3). For homogeneous, isotropic, incompressible, hydrodynamic turbulence, $s = \frac{2}{3}$ (Kolmogorov 1941; Obukhov 1941). To derive an analogous *Kolmogorov exponent*, s, from our obser-

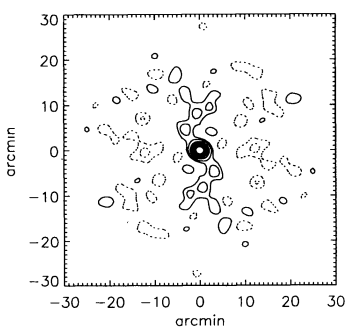

FIG. 4a

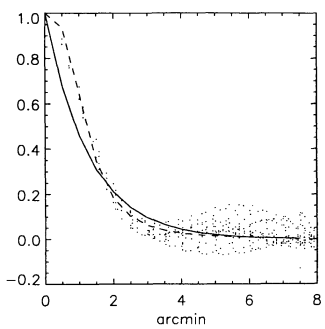

FIG. 4b

FIG. 4.—Similar to Fig. 2, but for the model data set described in § 2.2.3. On the left, (*a*) is shown a contour map of the two-dimensional biased autocorrelation function, and on the right, (*b*) we present exponential (*solid line*) and power-law (*dashed line*) fits to the azimuthally averaged ACF superposed on a scatter plot of the array values. The best-fit parameters are given in Table 3.

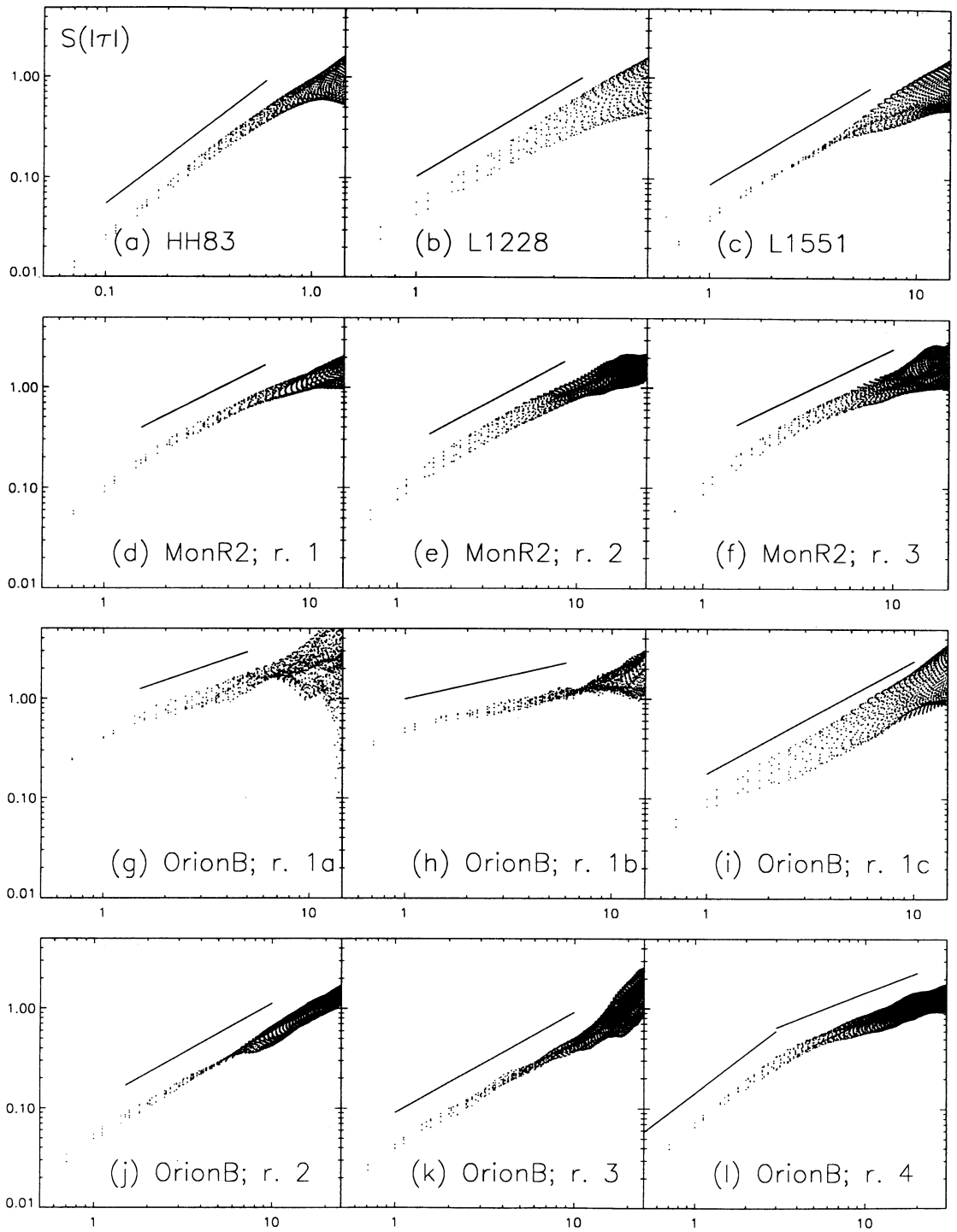

FIG. 5.—Logarithmic scatter plots of the observed one-dimensional unbiased structure functions with respect to the magnitude of their corresponding lag for the unfiltered data. The solid lines indicate the approximate slope of each azimuthally averaged structure function obtained via a linear least-squares fit, and the best-fit values are listed in Table 4.

vations, we have fitted each azimuthally averaged structure function to a power-law form and have overlayed the results on the scatter plots of Figures 5 and 6 (solid lines). The steep rise of the structure function at the smallest lags is most likely due to the effects of beam smoothing, and the innermost portions of the SFs in Figures 5 and 6 have therefore been excluded from the curve fits. It is important when calculating reliable power-law indices to do the fitting over a wide range of scales, so in all cases, we attempted to fit the data to a single power law, even where such a form seemed inappropriate (as in the filtered HH 83 data of Fig. 6*a*), simply to get a general idea of the scale properties of the fluctuations. An exception to this is the raw data for Orion B, region 4 (Fig. 5*l*), which exhibited two distinct spectral indices, and we have included both in Table 4, which also lists the best-fit indices for the remaining regions including the filtered data, the unfiltered data, and the

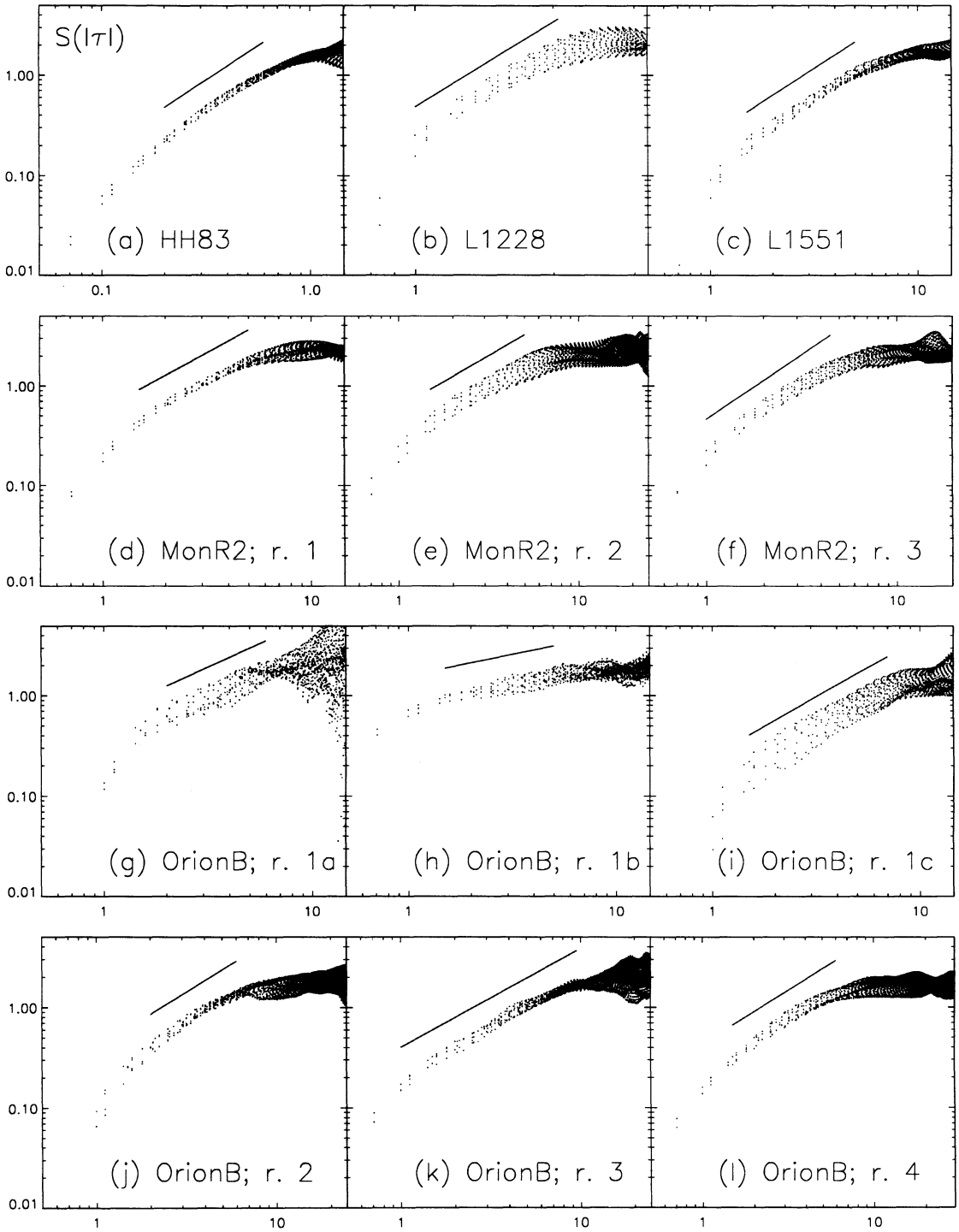

FIG. 6.—Similar to Fig. 5, but for the unfiltered data and including the noise correction given by eq. (B3). See Table 4 for the best-fit indices.

model. Figure 7 shows the one-dimensional structure function $S(|\tau|)$, for the model. The implications of these results will be discussed below (§ 5.3).

4.4. *Reynolds Stress and Turbulent Energy Transfer*

Small-scale turbulent velocity fluctuations, when superposed on more regular large-scale motions, will exert stresses on the mean flow that can, for example, help support a cloud against gravitational collapse. An understanding of how the turbulent (Reynolds) stress varies with scale is therfore necessary in order to determine the size range over which density concentrations are likely to become gravitationally unstable. If the velocity structure is isotropic and the density is assumed to be uniform, the scale variation of the turbulent pressure (i.e., of each of the

TABLE 4

KOLMOGOROV EXPONENTS[a]

Region	Unfiltered Data	Filtered Data
HH 83	1.57	1.37
L1228	1.41	1.47
L1551	1.22	1.34
Mon R2:		
1	1.05	1.13
2	0.97	1.04
3	0.94	1.29
Orion B:		
1a	0.71	0.95
1b	0.46	0.43
1c	1.13	1.17
2	1.00	1.10
3	1.00	0.98
4	1.30, 0.67	1.07
Model	1.37	...

[a] Derived from the unbiased structure functions.

diagonal elements of the Reynolds stress tensor) is given by (KD 1987)

$$\rho\sigma^2(L) = 3\rho\sigma_t^2(4/\pi)(N^2 - n^2)^{-1} \int\int_{\omega=\omega_L}^{\omega=\omega_{max}} P(\omega_x, \omega_y) d\omega_x d\omega_y , \quad (9)$$

where $P(\omega_x, \omega_y)$ is the power spectrum and $\omega = (\omega_x^2 + \omega_y^2)^{1/2}$ is the spatial frequency. For a discretely sampled data set on an $N \times N$ grid with spacing Δl, $L = n\,\Delta l$ and $\omega_L = N/2n$. The upper integration limit, ω_{max}, is just $N/2$. Thus, $\sigma^2(L)$ is a measure of the mean velocity dispersion of gas motions occurring inside a region of size L. It should be noted, however, that for compressible turbulence, density fluctuations can have an important influence on the Reynolds stress, so that the velocity dispersion calculated below may not be proportional to the turbulent pressure, as in the case of incompressible turbulence.

The estimator $\sigma^2(L)$ can also be used to obtain an approximate measure of the maximum rate at which energy can be transported, on average, on a given scale L by dividing the mean specific energy density of the turbulent motions on that scale, $3/2\sigma^2(L)$, by a characteristic time, $L/\sigma(L)$:

$$\epsilon(L) = \frac{3\sigma^3(L)}{2L} . \quad (10)$$

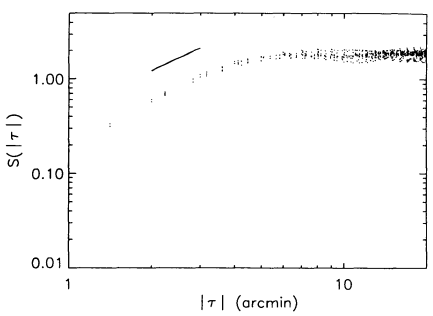

FIG. 7.—Logarithmic scatter plots of the type shown in Figs. 4 and 5 for the model data. The best-fit slope to the azimuthally averaged structure function is shown by the solid line and is listed in Table 4.

In the Kolmogorov-Obukhov scenario, turbulent energy is injected into the flow at some *outer* scale, λ_0, and drives the formation of smaller and smaller eddies until it is converted to thermal energy by molecular viscosity at a dissipation, or *inner* scale λ_i. This and similar cascade models predict the rate of energy transfer between scales, given by $\epsilon(L)$, to be constant within the *inertial subrange* defined by λ_i and λ_0. In actuality, $\epsilon(L)$ is an upper limit to the rate at which the energy present in turbulent eddies of size L can be transferred to other scales or, alternatively, can be dissipated and converted to thermal energy before any transfer between scales occurs. The peak value of $\epsilon(L)$, presented for each region in the caption to Figure 8, is therefore a measure of the maximum turbulent heating rate and can be used to evaluate the role of turbulence in the thermal balance of the clouds we have studied. The mean value for the maximum conversion rate of turbulent energy to thermal energy through dissipation is found to be $\approx 1.2 \times 10^{-4}$ ergs g^{-1} s^{-1}, which is comparable to the heating rate due to cosmic-ray ionization and dissociation of neutral hydrogen molecules, $\Gamma_{cr} \approx 1.9 \times 10^{-4}$ ergs g^{-1} s^{-1} (e.g., Spitzer 1978). However, if the turbulence is supersonic, dissipation in shock fronts may lead to localized heating, and the idea of an average dissipation rate would then be inaccurate. Thus, as above, the *latent* energy dissipation rate defined in equation (10) is only strictly applicable when the turbulence is incompressible (unless the dissipation rate is proportional to that in eq. [10], as is the case with the *dilatation* dissipation in compressible turbulence described by Zeman 1990).

Figure 8 shows $\sigma^2(L)$ (solid lines) and $\epsilon(L)$ (dotted lines) for each of the observed regions, and Figure 9 shows the same measures for the model data. We have presented only the results obtained from the raw velocity data because the filtered data looks similar on scales smaller than the half-width of the smoothing function (see Table 7). On larger scales, the $\sigma^2(L)$ curves for the filtered data flatten out, taking on constant values, while the $\epsilon(L)$ curves become inversely proportional to the scale, L. This is to be expected because the filtering process removes velocity components on scales larger than the width of the smoothing function, so the power spectra of the filtered maps vanish for small wavenumbers.

As discussed in detail by Kleiner & Dickman (1985), the variation of turbulent stress with scale, $\sigma^2(L)$, has important consequences for the gravitational collapse of density concentrations. Using order of magnitude estimates for the densities in each region [$n(H_2) \approx 1000$ for L1228 and L1551, 2500 for HH 83, 200 for Orion B, and 600 for Mon R2], we find that in all cases, the scale at which the turbulent dispersion, $\sigma(L)$, drops below the sound speed in the cloud is smaller than the thermal Jeans length [$\sim 25 n(H_2)^{-1/2}$ pc for a molecular cloud with a kinetic temperature of 10 K; shown in Fig. 8 as solid vertical lines]. This means that, in the regions we have studied, all clumps that are large enough to overcome their thermal pressure and collapse in the traditional Jeans analysis are instead supported by turbulent pressure. This conclusion is similar to that reported by Kleiner & Dickman (1987) and Hobson (1992), who invoke intermittency in the gas motions to account for the gravitational collapse and fragmentation that eventually leads to the formation of stars. The additional cloud support provided by magnetic fields further emphasizes the apparent need for an intermittent velocity structure to allow for gravitational instability. But note that these arguments are only strictly valid in the incompressible case, where the Reynolds stress is proportional to the $\sigma^2(L)$ estimator, as discussed

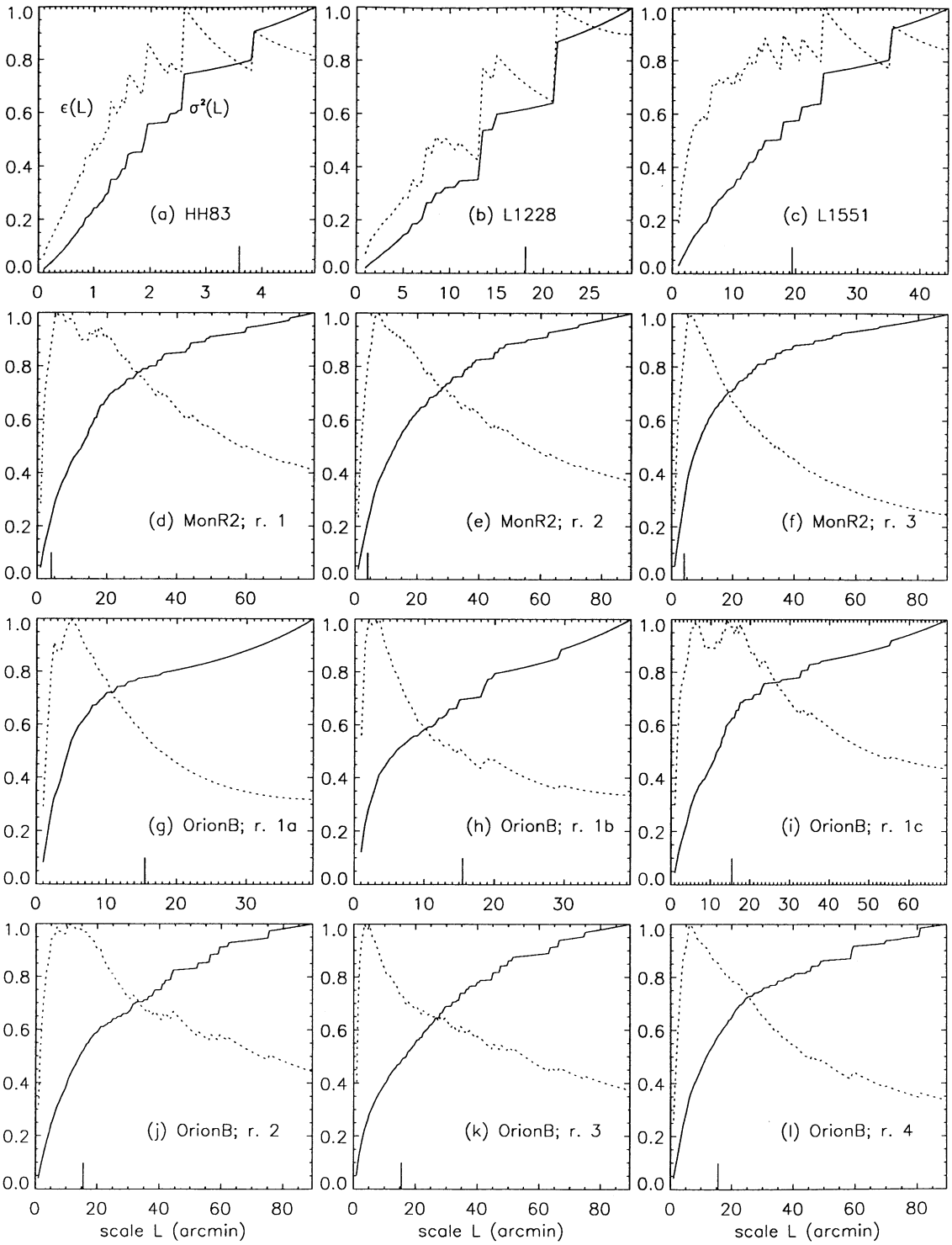

FIG. 8.—Specific turbulent energy density, $\sigma^2(L)$ (*solid lines*), and latent energy dissipation rate, $\epsilon(L)$ (*dotted lines*), as a function of scale for each region (*see text*). The solid vertical lines indicate the thermal Jeans length for each cloud assuming a kinetic temperature of 10 K and molecular hydrogen densities of 1000 for L1228 and L1551, 2500 for HH 83, 200 for Orion B, and 600 for Mon R2. Each of the $\sigma^2(L)$ curves is normalized with respect to its value at the maximum lag shown which is given approximately by the corresponding parent dispersion listed in Table 2, i.e., $\sigma^2(L_{max}) = \sigma_p^2$. The $\epsilon(L)$ curves are also given in terms of their maximum values, which are as follows: (*a*) HH 83; max $[\epsilon(L)] = 4.26 \times 10^{-5}$ ergs g^{-1} s^{-1}, (*b*) L1228; max $[\epsilon(L)] = 1.14 \times 10^{-4}$ ergs g^{-1} s^{-1}, (*c*) L1551; max $[\epsilon(L)] = 2.65 \times 10^{-5}$ ergs g^{-1} s^{-1}, (*d*) Mon R2, region 1; max $[\epsilon(L)] = 5.42 \times 10^{-5}$ ergs g^{-1} s^{-1}, (*e*) Mon R2, region 2; max $[\epsilon(L)] = 1.63 \times 10^{-5}$ ergs g^{-1} s^{-1}, (*f*) Mon R2, region 3; max $[\epsilon(L)] = 3.47 \times 10^{-5}$ ergs g^{-1} s^{-1}, (*g*) Orion B, region 1a; max $[\epsilon(L)] = 3.69 \times 10^{-5}$ ergs g^{-1} s^{-1}, (*h*) Orion B, region 1b; max $[\epsilon(L)] = 3.50 \times 10^{-5}$ ergs g^{-1} s^{-1}, (*i*) Orion B, region 1c; max $[\epsilon(L)]| = 5.26 \times 10^{-5}$ ergs g^{-1} s^{-1}, (*j*) Orion B, region 2; max $[\epsilon(L)] = 1.06 \times 10^{-4}$ ergs g^{-1} s^{-1}, (*k*) Orion B, region 3; max $[\epsilon(L)] = 7.14 \times 10^{-4}$ ergs g^{-1} s^{-1}, and (*l*) Orion B, region 4; max $[\epsilon(L)] = 2.02 \times 10^{-4}$ ergs g^{-1} s^{-1}.

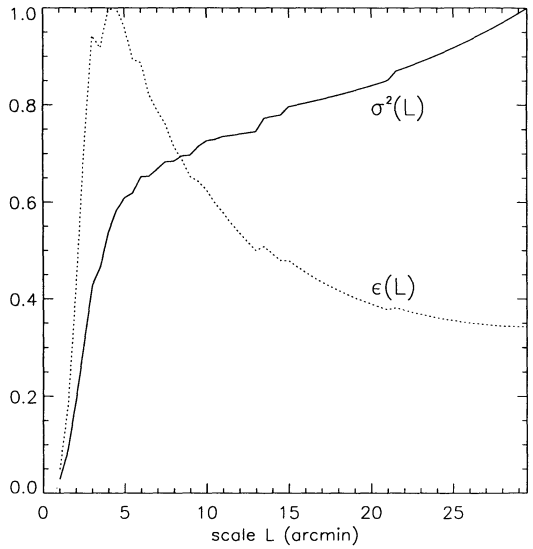

FIG. 9.—Similar to Fig. 8, but for the model data set

above. Compressibility effects could alter the turbulent pressure enough to make collapse possible even without intermittent velocity fluctuations.

The $\epsilon(L)$ curves in Figure 8 are also similar to those reported by Kleiner & Dickman (1987) and Hobson (1992) and, as they suggest, may indicate the existence of a preferred scale where the dissipation of turbulent energy is peaked, and where the resulting loss of dynamical support may lead to gravitational collapse. However, it is likely that the sharp drop at small scales in many of these plots [and for the $\sigma^2(L)$ measure as well] is an artifact of beam smoothing, and does not signify any real physical process occurring in the clouds (see § 5.1). Still, the secondary peaks found, for example, near the thermal Jeans length in Orion B, region 1c, and in Mon R2, region 1 do seem to reflect the actual scale variation of the $\epsilon(L)$ measure, marking a local peak in the latent energy transport rate on scales of several parsecs for these clouds.

5. DISCUSSION

5.1. *Beam Effects*

It is apparent from Figures 4, 7, and 9 that the spurious correlations introduced by beam smoothing (and enhanced slightly by the interpolation onto a regular grid, see § 2.2.3) extend beyond the angular width of the beam itself. In particular, Figure 4 shows that the effective correlation length for the otherwise random model velocity field is about equal to the simulated half-power beamwidth of 1.7 (§ 2.2.3), but beam-induced correlations of magnitude larger than 0.1 are present out to lags of more than 10′. Thus, the structure seen in many of the observed ACFs should be regarded with some skepticism. With this caveat in mind, it is nevertheless interesting to point out the roughly *chessboard* pattern of correlations and anticorrelations present in the residual L1228 map (Fig. 3*b*), possibly suggesting wave structure of some kind, and the recorrelations about 20′ from the center of Orion B, region 1, along the direction in which the small scale ACF is elongated (Fig. 3*g*).

Kitamura et al. (1993) have considered analytically the effect of beam smoothing on the observed ACF and find that the apparent velocity correlation length of a physical process after convolving the emission with a Gaussian radio telescope beam pattern will equal $(\lambda_c^2 + \theta^2/\ln 4)^{1/2}$, where λ_c is the true correlation length and θ is the beamwidth. For the model data set described above (§ 2.2.3), the underlying physical process is uncorrelated ($\lambda_c \ll \theta$), and the work of Kitamura et al. predicts an observed correlation length due solely to the beam, of 0.85(1.7) = 1.44. The slightly higher value of 1.5–1.6 that we have observed for our model can be attributed to the interpolation process (see § 2.2.3), and we thus find good agreement with the analytical result. However, note that the analytical work does not predict the spurious structure seen in Figure 4 at lags exceeding the beamwidth.

Beam smoothing also contaminates the structure function out to lags of over twice the beamwidth (Fig. 7), but possibly its most dramatic effect is on the $\sigma^2(L)$ and $\epsilon(L)$ measures shown in Figure 9. Spurious structure is seen in these curves at lags exceeding 10′, and the peak of the latent energy dissipation plot occurs at a relatively large lag of 4′. This casts some doubt on the validity of the $\sigma^2(L)$ and $\epsilon(L)$ results in particular for the HH 83 data (Fig. 8*a*), and the Orion B observations of regions 1a (Fig. 8*g*), 1b (Fig. 8*h*), and 3 (Fig. 8*j*). Note in particular the similarity between the curves in Figures 8*g* and 9. The model results also suggest that similar plots of the mean variance and the latent energy dissipation rate presented for Cloud 2 in Taurus by Kleiner & Dickman (1987) and for M17SW by Hobson (1992) may be dominated by beam effects and caution must be used in attaching to them any physical significance.

5.2. *Turbulent Length Scales*

We have listed the Kleiner & Dickman (1987) and the Hobson (1992) results for the correlation length, λ_c, with our own in Table 5. The correlation lengths are those derived from the biased ACFs of the noise-corrected filtered maps taken from Table 3. Also shown are the resolution of each study and the approximate extent of the region sampled. All scales are in parsecs, and the distances used for the conversions are given in the table along with their references. Note that in all cases, the observed (biased) correlation length is within roughly a factor of 2 of the beamwidth, and is in general 10–30 times smaller than the size of the region. This is also true for the LMC observations reported by Spicker & Feitzinger (1988a), even though the angular resolution was much larger (15′) and the scales involved (hundreds of parsecs) exceed those of the molecular cloud studies of Table 5 by several orders of magnitude. Furthermore, the correlation lengths listed in Table 3 do not decrease with distance as expected if the linear scale of velocity correlations were roughly the same in each of the clouds studied. On the contrary, the angular correlation lengths of Mon R2 (830 pc away) are comparable to or even larger than those of L1228, which is only about 150 pc distant. These results suggest that the observed correlation length for each of these objects is not a measure of any absolute, intrinsic scale characteristic of the flow, but is rather influenced by the length scales introduced by the observations themselves. This conclusion is verified by the work of Kitamura et al. (1993), who have presented a correlation analysis of TMC 1C, a subcondensation in Cloud 2, and have found that the observed correlation length increases approximately linearly with the size of the region being sampled.

The results listed in Table 5 can be understood if it is realized that the correlation length is related to the size of the largest velocity structures sampled by the observations because for any self-similar turbulent hierarchy, the correlation length

TABLE 5

CLOUD PARAMETERS

Region	Distance (pc)	Reference	Size (pc)	Half-Power Beamwidth (pc)	Biased Correlation Length (pc)
HH 83	480	Genzel et al. 1981	0.65	0.070	0.071
L1228	150	Fukuwi 1989	1.3	0.074	0.12
L1551	140	Elias 1978	1.8	0.069	0.15
Mon R2:					
1	830	Racine 1968	17	0.41	0.65
2			18	0.41	0.70
3			26	0.41	0.63
Orion B:					
1a	400	Anthony-Twarog 1982	1.8	0.20	0.20
1b			3.0	0.20	<0.20
1c			5.3	0.20	0.35
2			10	0.20	0.35
3			11	0.20	0.26
4			11	0.20	0.35
Cloud 2[a]	140	Kleiner & Dickman 1987	1.6	0.04	0.1
M17SW[b]:					
HCO^+	2200	Hobson 1992	1.7	0.20	0.25
HCN			1.7	0.20	<0.20

[a] Kleiner & Dickman 1987.
[b] Hobson 1992.

is related to the size of the largest "eddies" in the flow. For Kolmogorov turbulence within the inertial subrange, $\lambda_c \approx 0.47\lambda_o$, where λ_o is the outer scale, on which the turbulent motions are driven (Kleiner & Dickman 1985). Any astronomical observation of velocity structure in molecular clouds can only sample gas motions on scales larger than the resolution of the telescope and smaller than the extent of the sampling grid, or alternatively, the size of the cloud. If molecular cloud gas motions are part of a turbulent hierarchy pervading the interstellar medium and extending to much larger scales as originally proposed by Larson (1981), then the largest eddies sampled by any set of observations will be comparable to the extent of the data set, provided the scales introduced by the observations do not extend beyond the bounds of the hierarchy, and the observed correlation length will increase with the size of the region sampled. If the turbulence is self-similar, this increase will be linear. Similar conclusions were reached by Houlahan & Scalo (1990), who considered analytical models of hierarchical density structure and found that the correlation functions they calculated were strongly distorted by image features with sizes comparable to the extent of the data set. Thus, the apparent dependence of the observed correlation length on the size of the cloud discussed above and exhibited in Table 5 suggests that the observed motions are indeed part of a turbulent hierarchy, which at the very least pervades the molecular gas in the clouds we (and others) have surveyed. The question of whether the atomic gas surrounding the cloud is part of the hierarchy or not cannot be answered with molecular observations alone.

Kleiner & Dickman (1985) use the absence of any centroid velocity correlations at scales between 1 and 10 pc to argue against the existence of a turbulent hierarchy in the interstellar medium on scales comparable to or larger than the complex they observed (the Taurus dark clouds). However, as discussed by Scalo (1987), this only rules out an incompressible Kolmogorov-type cascade model and does not necessarily preclude the existence of a more complicated, highly compressible hierarchy for which an autocorrelation analysis will fail to discern any significant correlations if the dynamic range of the observations is insufficient. The dynamic range of the observations used by Kleiner & Dickman in their 1985 paper is about 56, smaller than that of most of the data sets presented here (note also that they did not observe the effects of beam smoothing presumably because their sampling interval was much larger than the spatial resolution of the telescope used).

If an interstellar turbulent hierarchy does exist, and if the intrinsic correlation length of the turbulence equals or exceeds the scale of our molecular cloud observations, then the calculations of Scalo (1984) and Dickman (1985) mentioned above (§ 2.2.2) imply that the effects of projection smearing should vanish and the observed dispersion in centroid velocities should approximate closely the true turbulent dispersion of the gas motions. We find that is not the case with our observations. The results listed in Table 2 show that the ratio of the observed centroid dispersion to the actual turbulent dispersion is given by $\sigma_{ct}^*/\sigma_t = 0.31 \pm 0.07$ for all the data sets listed with the exception of L1228 and Orion B, region 2 where the ratios are 0.13 and 0.42, respectively. This seems to imply that the correlation length of the turbulence does not exceed the scale of the observations, but instead, in all cases, lies between about 1% and 10% of the depth of the cloud, where the actual value depends on the scale properties of the flow (see Fig. 4 in Scalo 1984). This result is consistent with the sizes and correlation lengths listed in Table 5. However, as discussed above, if there is indeed a turbulent hierarchy of gas motions pervading the ISM, the correlation length derived from a finite range of scales within the effective range of the hierarchy is not an intrinsic scale of the turbulence, but instead depends on the size of the region being sampled. In the case of projection smearing, the range of scales being sampled is determined not by the scale of the observations, but by the depth of the emitting region. Thus, the projection effects discussed in § 2.2.2 depend only on the shape of the correlation function, and the correlation length used should be regarded as an *effective* correlation length

specific to the scale range sampled (the depth of the cloud) and determined by the functional form of the ACF or SF, rather than an absolute, characteristic, turbulent scale length.

5.3. *The Velocity Spectrum*

If the gas motions in molecular clouds are indeed part of an interstellar turbulent hierarchy, then observed *systematic* motions would actually be stochastic velocity fluctuations on scales comparable to the size of the data set, and any suppression of these by filtering would remove meaningful turbulent structure. However, the statistical approach described in § 2 could still be employed to characterize gas motions in scales smaller than the width of the filter. Therefore, in the case of sampling a turbulent hierarchy at some intermediate range in scales, the statistical analysis used here, although it cannot give information on absolute, characteristic length scales in the flow, can be used to obtain information on the form of the statistical functions, and as a result, the scaling laws we have derived do describe the physical nature of the hierarchy.

Although the correlation lengths for the biased ACFs of the filtered maps (Table 3) are not much larger than those of the model data set, it does seem clear from the best-fit exponents, n and s, and from the unbiased ACF results that the observed correlations are not due to beam smoothing alone, and instead reproduce the correlation properties of the underlying physical process responsible for the observed velocity fluctuations. In particular, with only a couple of exceptions, the filtered maps seem to be consistently well described by a power-law ACF with an exponent $n = 1.7 \pm 0.1$, which is significantly less than that found for the model, $n = 3.0$. It should be noted that even the two exceptions, L1228 and Orion B, region 1, exhibit a best-fit power law of ≈ 1.7 in the unfiltered maps (Table 3), and the higher value present in the filtered maps may be an indication that the noise correction for these regions (Table 2) is overestimated. The best-fit power-law exponents, n, for the raw velocity data exhibit a much larger variation than those of the unfiltered maps and are generally smaller, being characterized approximately by $n \approx 1.3 \pm 0.2$ (Table 3). The power-law exponents for both the filtered and unfiltered data are found to be independent of the size of the region. For H I gas motions in the Large Magellanic Cloud, Spicker & Feitzinger (1988a) report $n = 1.85 \pm 0.03$ for a radial cut to the biased ACF in the direction of the kinematical major axis. However, their results for the unbiased estimators and for radial cuts in other directions suggest larger exponents, $n \approx 2.5$ or in some cases exceeding 3 (see their Table 1).

The Kolmogorov exponents listed in Table 4 provide more useful measures of the scale properties of the turbulence than the power-law exponents, especially if the velocity structure arises from a turbulent cascade. In light of the smaller power-law exponents describing our observations, it is perhaps surprising that the Kolmogorov exponents, s, derived from the structure function are consistent with, but still slightly shallower than, those reported by Spicker & Feitzinger (1988a). They find an average value for s of 1.27 ± 0.21, with a minimum and maximum of 0.98 and 1.55 (see their Table 4), a range which spans most of our results exhibited in Table 4. Our derived exponents also agree well with the range $0.75 < s < 1.0$ which seems to characterize H II regions (Roy & Joncas 1985; Roy et al. 1986; Castañeda 1988; but see also O'Dell 1986 and O'Dell & Castañeda 1987, who find $s \approx 0.2$–0.4).

Despite this agreement, however, our Kolmogorov exponents are not consistent with those found in other molecular clouds using the autocorrelation function. Kleiner & Dickman (1987), report $s \approx 0.37$ in Heiles Cloud 2 for their raw data and $s \approx 0.15$ after filtering and applying the noise correction. Hobson (1992) finds somewhat higher values for M17SW, with $s \approx 0.33$ for his HCO^+ observations and $s \approx 0.52$ for HCN, but these are still much smaller than our results, with the possible exception of Orion B, region 1b. In order to investigate this discrepancy, we have calculated the Kolmogorov exponent, s, from the autocorrelation functions presented in § 4.2 by fitting both the biased and unbiased versions to the function form $C(|\tau|) = 1 - \alpha|\tau|^s$. For homogeneous isotropic turbulence and in the absence of systematic motions, this method should give an identical value for s to that obtained from the structure function. We find that the derivation of s using the ACF does indeed tend to give lower values, especially if the biased ACF estimator is used as in the Kleiner & Dickman (1987) and Hobson (1992) work. The mean Kolmogorov exponent derived via the unbiased structure function, using the raw (unfiltered) data summarized in Table 4, is 1.03 with a standard deviation of 0.31. The corresponding mean values obtained from the unbiased and biased ACFs are 0.85 and 0.60, respectively, with standard deviations of 0.26 and 0.23. The mean Kolmogorov exponents derived from the filtered data were found to be slightly steeper than, but still similar to, those describing the unfiltered data, suggesting that the turbulent velocity component dominates the small-scale structure of the SF even before systematic motions are removed. The filtered data give indices of 1.11 (using the unbiased structure function), 0.85 (using the unbiased ACF), and 0.63 (using the biased ACF) with standard deviations of 0.26, 0.24, and 0.24. Thus, the shallower slopes reported for other molecular cloud velocity fluctuation spectra may to some extent be the result of using the biased ACF to derive the Kolmogorov exponent rather than the unbiased structure function, as we have used here. Note, however, that even the slopes obtained from the biased ACFs presented here are steeper than those previously reported by Kleiner & Dickman (1987) and Hobson (1992).

It is well known that the biased ACF estimator decays to zero at large lags more slowly than the true ACF (Spicker & Feitzinger 1988b; Priestly 1981), so the shallower slope exhibited by that function is to be expected. The disagreement between the Kolmogorov exponents obtained from the autocorrelation and structure functions is probably due to the presence of small scale systematic trends in the velocity fields even after the smoothed maps were subtracted. As discussed above, the structure function is relatively insensitive to gradients and will therefore reproduce more accurately the true fluctuation spectrum. Alternatively, the steeper slopes found with the structure function could be attributed to projection smearing (§ 2.2.2; O'Dell & Castañeda 1987). For a process with a Kolmogorov-type spectrum ($s = \frac{2}{3}$), O'Dell & Castañeda show that projection smearing leads to an observed two-dimensional structure function with a spectral index of 5/3 if the effective correlation length of the turbulence is much less than the depth of the cloud, which is the case for our observations (see above). Taking all these effects into consideration, we find that the most reliable estimate for the spectral (Kolmogorov) slope, s, characterizing fluctuating gas motions in the molecular clouds we have surveyed is 0.86 ± 0.3.

It is interesting to compare this result with the predictions of some theoretical models of turbulent flows. As mentioned above, incompressible, homogeneous, isotropic turbulence

with no magnetic field yields a power-law form for the structure function with an index of $\frac{2}{3}$. Although this value is within the range given above for the observed scaling laws, our results do imply a somewhat steeper spectrum. In any case, the application of the Komogorov model to the supersonic gas motions typical of molecular clouds should be a priori suspect, and a more realistic interpretation of the observed scaling laws must include effects due to compressibility, magnetic fields, and self-gravity (Kleiner & Dickman 1985). When dealing with compressible turbulence, it is customary to break up the velocity field into solenoidal (incompressible) and potential (compressible) components that couple appreciably only on relatively large and small scales, and that can thus be considered approximately independently over a wide range in wavenumber (Pouquet, Passot, & Léorat 1991). In the absence of magnetic fields, the spectrum of the solenoidal component is that given by the Komogorov model modified by the presence of compressive modes and is characterized by a power-law index $s = 2/(3 - \mathcal{M}^2)$ for subsonic turbulence (rms Mach number $\mathcal{M} \leq 1$) (Moiseev et al. 1981). Intermittency effects may also act to steepen the velocity spectrum, but their importance is at present unclear (Kraichnan 1990). When $\mathcal{M}$ exceeds unity, shocks form and a Burgers-like spectrum prevails, where $s = 1$ for the potential and, when the coupling is sufficient, the solenoidal velocity components (Kadomtsev & Petviashvili 1973). Alternatively, if the solenoidal field is relatively strong, shock formation will be suppressed as acoustic waves efficiently diffuse along vortices, and the potential component will instead follow an $s = \frac{1}{2}$ power law (Zakharov & Sagdeev 1970; Passot, Pouquet, & Woodward 1988). A structure function index of $\frac{1}{2}$ is also predicted when Kolmogorov-like reasoning is applied to incompressible MHD flows (Kraichnan 1965). However, Grappin, Pouquet, & Léorat (1983) have shown that the spectral index of incompressible MHD turbulence can lie anywhere between $s = \frac{1}{2}$ and 2 depending on the degree to which velocity fluctuations are correlated with magnetic field fluctuations. Also note that turbulent MHD flows are typically characterized by several spectral indices spanning different ranges in wavenumber that depend on dissipation effects and the ratio of magnetic to kinetic energy (Zel'dovich, Ruzmaikin, & Sokoloff 1983). On large scales, where the magnetic energy is negligible, a Kolmogorov ($s = \frac{2}{3}$) spectrum prevails, while the Kraichnan result ($s = \frac{1}{2}$) holds on smaller scales, where the turbulent and magnetic energy are in equipartition. The influence of self-gravity has been considered in the self-similar star cloud turbulence model of Henriksen & Turner (1984), which predicts $s = 1$. In summary, the relation $\frac{2}{3} \leq s \leq 1.0$ is expected for the structure function spectral index in three-dimensional, compressible, hydrodynamic, self-gravitating turbulence, and $\frac{1}{2} \leq s \leq 2.0$ is expected in the MHD case. The analogous scaling laws in two spatial dimensions, which may, for example, apply to inhomogeneous turbulence pervaded by a strong magnetic field (Higdon 1984), are reviewed by Passot & Pouquet (1987). Many of these phenomenological results have been verified by numerical simulations (for a review, see Pouquet et al. 1991; see also the recent simulations of two- and three-dimensional supersonic hydrodynamic turbulence by Porter, Pouquet, & Woodward 1992 who find that shock wave interactions are important in the transfer of energy from small to large wavenumber within the inertial range for both the potential velocity component, which evolves to an $s = 1$ power law, and for the solenoidal component, which dominates the total kinetic energy at late times and, for the forced problem, is consistent with the Kolmogorov result, $s = \frac{2}{3}$).

The theoretical predictions agree well with those derived in the present work from the observed structure functions of radial velocity fluctuations in molecular clouds. In particular, they imply that compressibility effects are important in molecular clouds and that the weak acoustic model of Zakharov & Sagdeev (1970), which predicts $s = \frac{1}{2}$, is inapplicable. Also, if magnetic fields are indeed dynamically important, the observational results presented here may indicate a high degree of correlation between the turbulent velocity and magnetic field fluctuations in molecular clouds. An alternative interpretation due to Fleck (1983) is that, for a compressible medium in which the mean density scales with region size as $\rho l = \text{constant}$ (thought to be the case for molecular clouds; see Myers 1987), Komogorov-type reasoning leads to an expected spectral index $s = 4/3$ rather than $s = 2/3$. Since this is steeper than that observed, our results imply that compressibility effects that tend to steepen the spectrum are *less* significant then energy injection on small scales by, for example, young stars or supernovae, which will act to soften it.

Fleck's interpretation raises an important point. When comparing the observed scaling laws to theoretical cascade models, it must be remembered that inertial range arguments only apply in certain idealized situations and in particular are only strictly valid when the flow has reached a quasi-equilibrium state that is driven by a constant energy supply at some outer scale. In contrast, the interstellar medium is more likely described by decaying turbulence with energy injection on multiple scales, implying that traditional cascade models, although useful, should be applied with some caution. Note that the $\epsilon(L)$ curves of Figure 8 are certainly not consistent with the constant value assumed by many cascade models.

Our results for the Kolmogorov exponents can be used to derive a velocity dispersion region-size relationship of the type first described by Larson (1981): $\Delta v \propto l^{\gamma}$. Since a power-law structure function of the form $S(|\tau|) \propto |\tau|^s$ gives $\gamma = s/2$ (Kleiner & Dickman 1985), then the value of s given above implies $\gamma = 0.43 \pm 0.15$ for the molecular clouds in our survey, in agreement with observed indices obtained by other means, which suggests a value between 0.35 and 0.7 (e.g., Larson 1981; Myers 1987). Note in particular that Larson's (1981) original analysis, which included Orion A (where the HH 83 cloud is located), Orion B, Mon R2, and L1551 revealed an index of ≈ 0.38, which is close to that reported here. Figure 10 is a plot of velocity dispersion, Δv, versus region size, l, for all of the clouds we have studied. The dispersion for each cloud is defined as $\Delta v \equiv \sigma_c S'(l)^{1/2}$, where $S'(l)$ is the best-fit power law to the structure function of the filtered data (Table 4), σ_c is the centroid dispersion for the region (eq. [4]; Table 2), and l spans the range in scales over which the appropriate power-law fit was performed. The slope predicted by the Kolmogorov model is also shown for comparison. Note that the spectra at the smallest scales covered by our observations are slightly steeper than those at the largest, but otherwise the derived slopes, and more generally the functional forms of the ACFs and SFs, are very similar for all of the clouds we have studied. This implies that the hierarchy of gas motions in these clouds is approximately self-similar.

5.4. *Energy Injection and the Generation of Turbulence*

Turbulent flows are inherently dissipative and as such require a sustained supply of energy to maintain (Tennekes & Lumley 1972). As discussed above (§ 4.4), the minimum timescale, on average, for the dissipation of turbulent energy at some scale, L, is just $t_{\rm diss} \sim L/\sigma(L)$, where $\sigma(L)$ is a character-

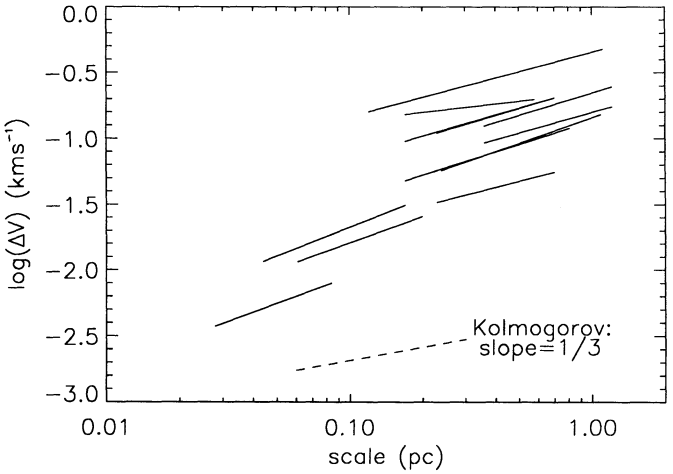

FIG. 10.—Velocity dispersion plotted vs. region size for all of the regions studied. The spectral indices and plot range for each object are those corresponding to the curve fits of Table 4, and Δv has been derived from power-law fits to the structure functions for the filtered data in each region and is defined in the text. The Kolmogorov slope is included for comparison.

istic velocity at that scale. Since the turbulence will decay unless energy is supplied at a rate comparable to or exceeding the dissipation rate, then, in order to sustain the observed motions, the timescale for energy injection into the flow, $t_{\rm inj}$, must be $\leq t_{\rm diss}$. If a source supplies turbulent energy at a rate $\dot{E}$, then $t_{\rm inj} = E(L)/\dot{E}$, where $E(L)$ is $1.5 M_c\, \sigma^2(L)$, and M_c and L are the mass and size of the cloud. Thus, the ratio of the energy injection timescale to the mean dissipation timescale is given by

$$\frac{t_{\rm inj}}{t_{\rm diss}} = 2.5 \times 10^{-4}\left[\frac{\sigma^3(L)}{L_{\rm pc}}\right]\left(\frac{M_c}{10^2\ M_\odot}\right)\left(\frac{\dot{E}}{100\ \mathscr{L}_\odot}\right)^{-1} \quad (11)$$

where $L_{\rm pc}$ is the cloud size in parsecs and $\sigma(L)$ is measured in km s^{-1}.

There are a variety of physical processes that inject energy into the interstellar medium, and some of the most important are summarized in Table 6 along with the approximate scale range over which they operate and the rate at which they supply turbulent energy (for a more detailed discusson of several of these injection mechanisms, see Bally et al. 1991). Each rate includes an efficiency factor, η, which reflects how effective the mechanism is in converting the energy it liberates into interstellar turbulent motions. We will not attempt a calculation of the efficiency factors here, but for a treatment of the conversion process, see, for example, Miesch & Zweibel (1994). The size, mass, and surface area of the cloud are denoted by L_c, M_c, and A_c, respectively, in Table 6, and for those processes that drive "bubbles" of hot gas into the surrounding ISM (supernova, stellar winds, and H II regions), Ω_c is the solid angle of the cloud as seen from the center of the bubble. Characteristic timescales for several mechanisms (e.g., the free-fall time for gravitational torques) are represented by t, and N represents the total number of outflows, hot stars, or supernovae injecting energy into the cloud. For example, consider a supershell driven by multiple supernovae from an OB association. In this case, the number of stars in the association that have exploded as supernovae ($\sim$20) is denoted by N, the timescale for any particular region of the ISM to be traversed by such a supershell ($\sim$30 Myr for the solar neighborhood) is denoted by t, and Ω_c is the solid angle of the cloud as seen from the center of the association ($\sim$0.1). The energy liberated by a single supernova is represented by $E_{\rm SN}$. A typical velocity for the postshock gas after the passage of a spiral density wave in the solar neighborhood is $\Delta V \sim 10$ km s^{-1} (Spitzer 1978), and $V_{\rm flow}$ and $V_{\rm wind}$ are characteristic outflow and stellar wind velocities. The mass of a particular outflow is given by $M_{\rm flow}$, and $\dot{M}$ is the mass-loss rate in a typical stellar wind. Other symbols found in Table 6 include the number of ionizing photons from the central star in an H II region, Q, the ultraviolet radiation flux incident on a typical molecular cloud, $X_{\rm UV}$, and the spiral density wave pattern frequency, Ω_p ($\sim 1.4 \times 10^{-8}$ yr^{-1}; Spitzer 1978).

Using equation (11) together with the observed relation between the density and size of typical molecular clouds, $n \approx 4 \times 10^3 L_{\rm pc}^{-1.2}$ (Scalo 1987), and our results for the variation of the specific energy density, $1.5\sigma^2(L)$, with scale (§ 4.4), we find that the maximum value of $t_{\rm inj}/t_{\rm diss}$ for all the clouds we have surveyed occurs in Orion B, region 3, and is equal to 0.015(100 $\mathscr{L}_\odot/\dot{E}$). Since this value is less than unity for any source supplying turbulent energy at a rate $\dot{E} \geq 1.5\ \mathscr{L}_\odot$, we find that a number of valid energy injection mechanisms exist which could account for the observed turbulent motions in molecular clouds on all scales, from 0.01 pc to the size of the cloud, L_c (see Table 6). This conclusion can be made even more general if we employ the size–line width and size–density scaling laws first introduced by Larson (1981). If the velocity dispersion and the density of a region scale with its size as $\sigma(L) = \sigma_0 L_{\rm pc}^{\gamma}$ and $n = n_0 L_{\rm pc}^{\beta}$, then equation (11) implies

$$\frac{t_{\rm inj}}{t_{\rm diss}} = 2.5 \times 10^{-4} L_{\rm pc}^{3\gamma+\beta+2}\left(\frac{\sigma_o}{1\ {\rm km\ s^{-1}}}\right)^3 \times \left(\frac{M_o}{10^2\ M_\odot}\right)\left(\frac{\dot{E}}{100\ \mathscr{L}_\odot}\right)^{-1}, \quad (12)$$

where $M_o \equiv (4\pi/3)(1\ {\rm pc}/2)^3(2m_{\rm H})n_o$. Using the observed parameter values of $\sigma_o = 1.0$ km s^{-1}, $n_o = 4 \times 10^3$ cm^{-3}, $\gamma = \frac{1}{2}$, and $\beta = -1.2$ (Scalo 1987), equation (12) yields

$$\frac{t_{\rm inj}}{t_{\rm diss}} = 2.6 \times 10^{-4} L_{\rm pc}^{2.3}\left(\frac{\dot{E}}{100\ \mathscr{L}_\odot}\right)^{-1}. \quad (13)$$

The value of γ derived in the present work, 0.43 ± 0.15 (§ 5.3) gives $t_{\rm inj}/t_{\rm diss} \propto L_{\rm pc}^{2.09}/\dot{E}$. Thus, the energy sources of Table 6 are certainly sufficient to sustain small-scale turbulent motions, but in order to drive turbulence at scales larger than the size of a typical giant molecular cloud ($\sim$40 pc), an energy injection rate exceeding 100 $\mathscr{L}_\odot$ is required. Since the energy injection mechanisms that act on the scale of the cloud—UV radiation, Galactic differential rotation, spiral density waves, and gravitational torques—supply more energy as the cloud size is increased, then these processes may still be sufficient to maintain a turbulent hierarchy in the ISM extending to much larger scales (recall also that $t_{\rm diss}$ is a *minimum* dissipation timescale). Alternatively, if the turbulence is anisotropic, then large-scale turbulent motions could be driven by small-scale energy injection. The question of whether such an inverse energy cascade exists in the interstellar medium or whether a more traditional Kolmogorov-type energy cascade from small to large wavenumber prevails is still an open one.

6. SUMMARY

We have presented a statistical analysis of ^{13}CO emission line centroid velocity fluctuations for five nearby molecular

TABLE 6

GENERATION OF TURBULENCE IN MOLECULAR CLOUDS[a]

Source	Scale (pc)	Energy Injection Rate[b] ($\mathscr{L}_\odot$)
Bipolar outflows	0.1–1	$40\left(\frac{\eta}{0.5}\right)\left(\frac{N}{10}\right)\left(\frac{M_{\rm flow}}{5\ M_\odot}\right)\left(\frac{V_{\rm flow}}{10\ {\rm km\ s^{-1}}}\right)^2\left(\frac{t}{10^4\ {\rm yr}}\right)^{-1}$
H II regions	0.01–20	$56\left(\frac{\eta}{0.01}\right)\left(\frac{Q}{10^{48}\ {\rm s^{-1}}}\right)\left(\frac{\Omega_c}{4\pi}\right)$
Isolated supernovae	1–20	$162\left(\frac{\eta}{0.01}\right)\left(\frac{E_{\rm SN}}{10^{51}\ {\rm ergs}}\right)\left(\frac{\Omega_c}{4\pi}\right)\left(\frac{t}{0.5\times10^6\ {\rm yr}}\right)^{-1}$
Stellar winds	1–50	$1.3\left(\frac{\eta}{0.1}\right)\left(\frac{N}{10}\right)\left(\frac{\dot{M}}{10^{-6}\ M_\odot\ {\rm yr^{-1}}}\right)\left(\frac{V_{\rm wind}}{10^3\ {\rm km\ s^{-1}}}\right)^2\left(\frac{\Omega_c}{0.1}\right)$
Supershells	150–200	$0.4\left(\frac{\eta}{0.01}\right)\left(\frac{N}{20}\right)\left(\frac{E_{\rm SN}}{10^{51}\ {\rm ergs}}\right)\left(\frac{\Omega_c}{0.1}\right)\left(\frac{t}{30\times10^6\ {\rm yr}}\right)^{-1}$
UV Radiation[c]	$\sim L_c$	$59\left(\frac{\eta}{0.001}\right)\left(\frac{X_{\rm UV}}{10G_o}\right)\left(\frac{A_c}{1500\ {\rm pc^2}}\right)$
Galactic shear	$\sim L_c$	$0.08\left(\frac{\eta}{1.0}\right)\left(\frac{M_c}{10^5\ M_\odot}\right)\left(\frac{L_c}{40\ {\rm pc}}\right)^2$
Spiral density waves	$\sim L_c$	$2.3\left(\frac{\eta}{0.1}\right)\left(\frac{M_c}{10^5\ M_\odot}\right)\left(\frac{\Delta V}{10\ {\rm km\ s^{-1}}}\right)^2\left(\frac{\Omega_p}{1.4\times10^{-8}\ {\rm yr^{-1}}}\right)$
Graviational torques	$\sim L_c$	$35\left(\frac{\eta}{0.1}\right)\left(\frac{M_c}{10^5\ M_\odot}\right)^2\left(\frac{L_c}{40\ {\rm pc}}\right)^{-1}\left(\frac{t}{10^6\ {\rm yr}}\right)^{-1}$

[a] See text for the definitions of the symbols.
[b] Each injection rate is given in units of the solar luminosity.
[c] The ultraviolet flux incident on the cloud, $X_{\rm UV}$, is given in terms of the Habing flux, $G_o = 1.6 \times 10^{-3}$ ergs cm^{-2} s^{-1} (see Tielens & Hollenbach 1985).

clouds; Orion B, Mon R2, L1228, L1551, and the HH 83 cloud, and our primary conclusions are as follows:

1. The model data cubes described in § 2.2.3 reveal that the effects of beam smoothing are more pronounced than might be naively expected, extending beyond the width of the beam itself (§ 5.1). The innermost portions of the statistical diagnostics we have presented are certainly influenced by the telescope's resolution, and similar measures previously reported in the literature also seem to be polluted by beam effects at very small scales.

2. The observed variation of turbulent pressure with region size implies that, on scales where the turbulent stress is small, thermal pressure is sufficient to support density condensations against collapse, and on scales that are unstable in the traditional thermal Jeans analysis, the turbulent pressure assumes the role of cloud support (§ 4.4). Thus, intermittency in the velocity field or compressibility effects on the turbulent pressure may be required to produce gravitational instability.

3. The turbulent length scales presented in § 4.2 for our data, and those presented by other authors, are strongly dependent on the range of scales sampled by the observations. We suggest that this, together with the observed similarity between the functional forms of the ACFs and SFs for different data sets, may be evidence for a self-similar turbulent hierarchy of gas motions extending over a wide range of scales in the interstellar medium (§ 5.2). The scale invariance of the hierarchy implies that the normalized statistics of the velocity structure, limited by observational selection to a particular wave number band in the effective inertial range (or, more generally, the range of the hierarchy), will be identical regardless of the absolute scale. Thus, correlation lengths and any other scales derived from the observed correlation functions, such as integral scales or Taylor microscales, can describe the self-similar form of the true ACFs and SFs, but in the band-limited case, cannot give information on any absolute, intrinsic length scales of the flow. This observational selection must be considered in correctly interpreting the results of statistical analyses similar to that described here.

4. The mean power-law index (or Kolmogorov exponent) describing the observed velocity spectra is found to be $s \approx 0.86 \pm 0.3$ (§ 5.3). This is consistent with phenomenological predictions for isotropic turbulence when the effects of compressibility, magnetic fields, and self-gravity are taken into account. This index implies a size–velocity dispersion relation of the form $\Delta v \propto l^\gamma$, with $\gamma \approx 0.43 \pm 0.15$, which agrees with the range found by other studies and derived by different means, $0.35 < \gamma < 0.7$ (e.g., Larson 1981; Myers 1987). Our value is also in approximate agreement with that describing velocity fluctuations in H II regions, but is significantly steeper than that found in similar correlation studies for other molecular clouds by Kleiner & Dickman (1987) and Hobson (1992).

5. We have considered the generation of turbulence on different length scales in the interstellar medium and find that there exist a number of physical processes that can supply energy at a rate sufficient to sustain the gas motions observed in molecular clouds (§ 5.4).

Although scaling laws and other useful information can be obtained from the ACF and SF, the beam smoothing and selection effects found in the present work do limit the utility of the approach in characterizing molecular cloud gas motions. In addition, correlation functions are known to be incomplete in their description of turbulence and to suffer from "leakage" effects, projection smearing, edge effects, and other geometrical difficulties, all of which can lead to a misrepresentation of the

underlying flow (Cantwell 1981; Jenkins & Watts 1968; Houlahan & Scalo 1990). For these reasons, we do not recommend the use of the two-point statistical analysis presented here in quantitatively characterizing either the column density or the centroid velocity structure of molecular cloud observations. A more fruitful statistical approach may be to study the form of the probability distribution of the centroid velocities and their spatial derivatives. In a forthcoming paper, we consider these probability distributions of the same data sets described here (Scalo & Miesch 1994). Other alternatives include the power spectra approach of Kitamura et al. (1993), the triangle transformations introduced by Langer, Wilson, & Anderson (1993), or the wavelet analysis described by Gill & Henriksen (1990).

We would like to extend our gratitude to J. M. Scalo for a number of suggestions that have improved the presentation and the content of the paper and E. G. Zweibel and P. Fox for helpful discussions and comments. We also thank Ron Miller for supplying the Pb SIS junctions that made the excellent observations possible during the middle 1980s. We thank Dennis Mumma for his efforts in keeping the 7 m antenna trouble free and operational and Robert W. Wilson who wrote most of the data reduction software used to process data taken with the Crawford Hill 7 m telescope. The vision of Arno Penzias and Robert W. Wilson allowed the 7 m telescope to produce the molecular cloud surveys on which this and other papers are based. We thank Aron Kranhert, Marc Pound, and Greg Wright for help with the data acquisition and for helping to realize automatic observing with the 7 meter. Robert W. Wilson and William D. Langer provided much scientific insight, encouragement, and motivation during the data acquisition phase of this project.

APPENDIX A

FILTERING

The validity of the statistical analysis presented here depends on the assumption of stationarity and therefore requires the removal of any nonstationary velocity components from the data (§ 2.1). With this in mind, we have applied several low-pass filters to the centroid maps to extract systematic motions such as those arising from the rotation of the cloud. The filtering is accomplished by convolving the data with a smoothing function, and then subtracting the smoothed map from the original to obtain the residual *fluctuating* velocity component, which is then subjected to the correlation analysis. The convolution procedure is to be preferred over simply fitting a polynomial surface to the data because such a fit necessarily imposes structure onto the map that may not actually be present.

For the present work, we have employed two different smoothing functions, presented in Figure 11*a* for one particular choice of the filter widths. The functions themselves are two dimensional, and we have plotted only a one-dimensional cross section versus grid spacing, with the origin of the ordinate corresponding to the center point of the smoothing function. The first (represented by the solid line) is an equally weighted moving average filter, which is simply a square two-dimensional step function in the spatial domain. The dashed line corresponds to the smoothing function originally developed for geophysical applications by Zurflueh (1967, which we will refer to hereafter as the *Zurflueh filter*). The frequency response of the filters is exhibited in Figure 11*b*, which shows one-dimensional slices through the Fourier transform of each smoothing function as a function of spatial frequency in units of cycles per unit of grid spacing. Clearly, the latter has the more desirable response, approximating a step function in the frequency domain to a higher degree than the former, and avoiding negative values that reverse the polarity of spatial frequency components and that can, as a result, introduce spurious high-frequency ripples into the smoothed output (Holloway 1958). In addition, the symmetry of the Zurflueh filter implies that it introduces no spurious phase shifts, unlike the moving average filter (Zurflueh 1967).

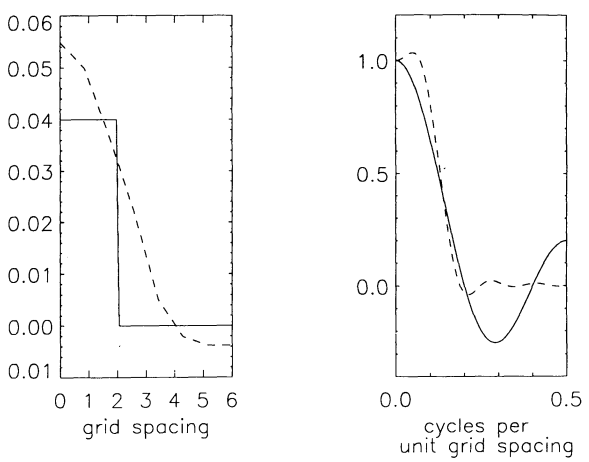

FIG. 11.—One-dimensional slices through the spatial (*a*) and frequency (*b*) response of the two smoothing functions used to filter out small-scale structure in the centroid velocity maps. The solid line represents an equally weighted moving average filter with a half-width of 2, and the dashed line corresponds to the original Zurflueh filter (see text) having a half-width of 6. The smoothing function itself is normalized such that the array of weighing coefficients that defines the filter sum to unity and the frequency response is given in terms of its value at zero frequency.

TABLE 7

OPTIMAL FILTERS

Region	Type	Half-width (grid units)	Half-width
HH 83	Zurflueh	42	2.1
L1228	Zurflueh	24	12.0
L1551	Zurflueh	36	18.0
Mon R2:			
1	Moving average	20	10.0
2	Moving average	20	10.0
3	Moving average	20	10.0
Orion B:			
1a	Zurflueh	30	15.0
1b	Zurflueh	30	15.0
1c	Zurflueh	30	15.0
2	Moving average	20	10.0
3	Moving average	25	12.5
4	Moving average	25	12.5

For these reasons, the Zurflueh filter was also used, and recommended, by Spicker & Feitzinger (1988a, b) in their study of H I gas motions in the LMC.

Despite the numerous advantages of the Zurflueh filter over the moving average filter in principle, we find little difference between the two in practice when applied to our data sets. Since roughly the same degree of smoothing can be achieved with a smaller convolving array in the case of the moving average filter (Fig. 11), the application of this filter is more computationally efficient and for this reason has been implemented for our largest data sets (see Table 7).

The optimal smoothing function for each region was found by applying filters of various widths, beginning with the widest and decreasing the width until the anticorrelated sidelobes, characteristic of large-scale gradients (see § 4.2), were no longer discernible in the autocorrelation function of the residual velocity map. Such a procedure is rather qualitative and imprecise, but we find that our conclusions are insensitive to the precise value chosen for the optimal filter width. To achieve the desired cutoff wavelengths for the Zurflueh filter, we have constructed a series of wider smoothing functions through bilinear interpolation of the 8 unit filter originally presented by Zurflueh (1967). In the same paper, Zurflueh finds that the properties of the filters he developed are insensitive to effects of interpolation and grid spacing, so that our wider filters should retain the general characteristics of the originals. The optimal filter width chosen for each region is listed in Table 7 along with the type of filter used (see § 3.1 for the region definitions).

When applying these filters, it is more computationally efficient to carry out the convolution process in the frequency domain, where it becomes simply a product between the Fourier transform of the smoothing function and that of the velocity map. Instead we have chosen to do the filtering solely in the spatial domain because, despite its disadvantages in terms of efficiency, it enables us in each map to treat the pixels where there is no significant emission as nulls, rather than zeros, and thus ignore those pixels when computing the spatial integration of the convolution kernal. Such a procedure is impossible to carry out if the filter is applied in the frequency domain. In addition, it is more straightforward to extract both the systematic and the fluctuating components from the centroid maps when Fourier transforms are avoided.

APPENDIX B

INSTRUMENTAL NOISE CORRECTIONS FOR THE ACF AND SF

Following Dickman & Kleiner (1985), we define the noise-induced error in the observed centroid velocity of an emission line as $\delta v_c(\boldsymbol{r}) \equiv v_c(\boldsymbol{r}) - v_c^*(\boldsymbol{r})$, where $v_c(\boldsymbol{r})$ is the measured value obtained using equation (5), and $v_c^*(\boldsymbol{r})$, is the value which would have been obtained in the absence of instrumental noise. The error, $\delta v_c(\boldsymbol{r})$, is expected to be randomly distributed with zero mean and a variance which we denote as σ_n^2. If it is also spatially uncorrelated and independent of the actual value of the centroid velocity, $v_c^*(\boldsymbol{r})$, then the observed centroid variance, defined in equation (4), is given by

$$\sigma_c^2 = (\sigma_c^*)^2 + \sigma_n^2 , \tag{B1}$$

where $\sigma_c^{*2} \equiv \langle v_c^{*2}(\boldsymbol{r}) \rangle$ is the noise-free variance.

White noise manifests itself in the autocorrelation function as a spike at the origin and, when superposed on the noise-free ACF (and renormalized to ensure that the ACF is unity at $\tau = \mathbf{0}$), leads to an underestimation of the true correlations at nonzero lags. Thus, in the presence of instrumental noise giving rise to a centroid variance of σ_n^2 as described above, it is necessary to apply a correction to the ACF at nonzero lags of the form (DK 1985)

$$C^*(\tau) = \frac{C(\tau)}{1 - (\sigma_n/\sigma_c)^2} \quad \tau \neq 0 \tag{B2}$$

to obtain the noise-free autocorrelation function, $C^*(\tau)$. A similar analysis of the effects of instrumental noise on the structure function gives

$$S^*(\tau) = \frac{S(\tau) - 2(\sigma_n/\sigma_c)^2}{1 - (\sigma_n/\sigma_c)^2} \quad \tau \neq 0 \tag{B3}$$

for the noise correction [with $S(\mathbf{0}) \equiv 0$ by definition].

In order to apply equations (B2) and (B3), it is first necessary to estimate the noise variance, σ_n^2. This can be done in several ways (DK 1985), but the most straightforward is to create a large number of model Gaussian spectra whose center velocities vary randomly with a normal probability distribution having a standard deviation equal to σ_c^*. If artificial white noise is then added to each line, and the new centroid velocities are calculated, the total centroid dispersion, σ_c, can be obtained from the statistical properties of the ensemble of model spectra. The model dispersion, σ_c^*, can be adjusted until the simulations reproduce the observed centroid variance given by equation (4). The nose variance then follows directly from equation (B1); $\sigma_n^2 = \sigma_c^2 - \sigma_c^{*2}$. We have computed the noise variance in this manner and have checked the result for each cloud using the approximate relation given by Dickman & Kleiner (1985, their eq. [67]). The two methods agreed in all cases to within 10%.

The noise-induced error in the centroid velocity for each iine, $\delta v_c(r)$, and in turn the noise variance, σ_n^2, will in general depend on the signal-to-noise ratio, the line width, the spectral resolution, and the number of spectrometer channels over which the summation in (3) is carried out (DK 1985). For the average line width, which is equivalent to the *internal* velocity dispersion defined by DK 1985, and which will be denoted as σ_i, we have considered several independent means of estimation, including the direct calculation (KD 1985, eq. [20]) and an estimate based on the area under the line and the assumption that it is approximately Gaussian (Kleiner & Dickman 1985, eq. [18]). However, we find from numerical simulations of model lines superposed with Gaussian noise (and from insight obtained by studying the ensemble mean spectra) that more reliable estimates can be obtained by actually fitting a Gaussian to each spectral line or by counting the number of channels in which the brightness temperature exceeds 50% of its maximum value to obtain the FWHM for each line, which is in turn proportional to the dispersion. For the more complicated regions (such as Orion B), where the lines were not in general single-component Gaussians and where their shapes often varied across the map, it was difficult to define an average linewidth or dispersion and, for this reason, we estimate that the noise variances are uncertain to as much as 20%.

As a final note, for maps composed of a juxtaposition in space and velocity of several subregions (see the discussion of Orion B, § 3.1) we find that the noise corrections are simply given by equations (B2) and (B3) with σ_n^2 replaced by an effective noise variance that is equal to the average of the noise variances in each subregion weighed by the number of pixels (excluding null pixels).

REFERENCES

Anthony-Twarog, B. J. 1982, AJ, 87, 1213
Bally, J., Castets, A., & Duvert, G. 1994, ApJ, 423, 310
Bally, J., Langer, W. D., Wilson, R. W., Stark, A. A., & Pound, M. W. 1991, in IAU Symp. 147, Fragmentation of Molecular Clouds and Star Formation, ed. E. Falgarone, F. Boulanger, & G. Duvert (Dordrecht: Kluwer), 11
Bally, J., Stark, A. A., Wilson, R. W., & Henkel, C. 1987, ApJ, 65, 13
Bracewell, R. 1965, The Fourier Transform and its Applications (New York: McGraw-Hill)
Cantwell, B. J. 1981, Ann. Rev. Fluid Mech., 13, 457
Castañeda, H. O. 1988, ApJS, 67, 93
Castets, A., Duvert, G., Dutrey, A., Bally, J., Langer, W. D., & Wilson, R. W. 1990, A&A, 234, 469
Chappell, D., & Scalo, J. 1993, preprint
Dickman, R. L. 1985, in Protostars and Planets II, ed. D. C. Black & M. S. Matthews (Tucson: Univ. Arizona Press), 150
Dickman, R. L., & Kleiner, S. C. 1985, ApJ, 295, 479 (DK 1985)
Edelson, R. A., & Krolik, J. H. 1988, ApJ, 333, 646
Elias, J. H. 1978, ApJ, 224, 857
Falgarone, E., Phillips, T. G., & Walker, C. K. 1991, ApJ, 378, 186
Fleck, R. C. 1983, ApJ, 272, L45
Fukuwi, Y. 1989, in Proc. ESO Workshop on Low Mass Star Formation and Pre–Main-Sequence Objects, ed. B. Reipurth (Garching: ESO)
Genzel, R., Reid, M. J., Moran, J. M., & Downes, D. 1981, ApJ, 244, 884
Gill, A. G., & Henriksen, R. N. 1990, ApJ, 365, L27
Grappin, R., Pouquet, A., & Léorat, J. 1983, A&A, 126, 51
Henriksen, R. N. 1988, ApJ, 331, 359
———. 1991, in IAU Symp. 147, Fragmentation of Molecular Clouds and Star Formation, ed. E. Falgarone, F. Boulanger, & G. Duvert (Dordrecht: Kluwer), 83
Henriksen, R. N., & Turner, B. E. 1984, ApJ, 287, 200
Henry, P. S. 1976, Rev. Sci. Instr., 47, 1020
Higdon, J. C. 1984, ApJ, 285, 109
Hobson, M. P. 1992, MNRAS, 256, 457
Holloway, J. L. 1958, Adv. Geophys., 4, 351
Houlahan, P., & Scalo, J. M. 1990, ApJS, 72, 133
Jenkins, G. M., & Watts, D. G. 1968, Spectral Analysis and its Applications (San Francisco: Holden-Day)
Kadomtsev, B. B., & Petviashvili, V. I. 1973, Soviet Phys. Dokl., 18, 115
Kaplan, S. A. 1966, Interstellar Gas Dynamics (2d ed.; Oxford: Pergamon)
Kaplan, S. A., & Klimishin, I. A. 1964, Soviet Astron., 8, 210
Kitamura, Y., Sunada, K., Hayashi, M., & Hasegawa, T. 1993, ApJ, 413, 221
Kleiner, S. C., & Dickman, R. L. 1984, ApJ, 286, 255
Kleiner, S. C., & Dickman, R. L. 1985, ApJ, 295, 466
———. 1987, ApJ, 312, 837 (KD 1987)
Kolmogorov, A. N. 1941, Dokl. Akad. Nauk SSR, 30, 301
Kraichnan, R. H. 1965, Phys. Fluids, 8, 1385
———. 1990, Phys. Rev. Lett., 65, 575
Langer, W. D., Wilson, R. W., & Anderson, C. H. 1993, ApJ, 408, L45
Larson, R. B. 1981, MNRAS, 194, 809
Léorat, J., Passot, T., & Pouquet, A. 1990, MNRAS, 243, 293
Miesch, M. S., & Zweibel, E. G. 1994, ApJ, in press
Moiseev, S. S., Petviashvili, V. I., Toor, A. V., & Yanovsky, V. V. 1981, Physica 2D, 218
Myers, P. C. 1987, in Interstellar Processes, ed. D. J. Hollenbach & H. A. Thronson (Dordrecht: Reidel), 71
Narayan, R. 1988, in AIP Conf. Proc. 174, Radio Wave Scattering in the Interstellar Medium, ed. J. M. Cordes, B. J. Rickett, & D. C. Backer (New York: AIP), 17
Obukhov, A. M. 1941, Izv. Akad. Nauk SSR, Ser. Geograf. i. Goefiz., Nos. 4–5, 453
O'Dell, C. R. 1986, ApJ, 304, 767
O'Dell, C. R., & Castañeda, H. O. 1987, ApJ, 317, 686
Passot, T., & Pouquet, A. 1987, J. Fluid Mech., 181, 441
Passot, T., Pouquet, A., & Woodward, P. 1988, A&A, 197, 228
Pérault, M., Falgarone, E., & Puget, J. L. 1986, A&A, 157, 139
Porter, D. H., Pouquet, A., & Woodward, P. R. 1992, Theor. Comput. Fluid Dyn., 4, 13
Pound, M. W., Bania, T. M., & Wilson, R. W. 1990, ApJ, 351, 165
Pouquet, A., Passot, T., & Léorat, J. 1991, in IAU Symp. 147, Fragmentation of Molecular Clouds and Star Formation, ed. E. Falgarone, F. Boulanger, & G. Duvert (Dordrecht: Kluwer), 101
Press, W. H., Flannery, B. P., Teukolsky, S. A., & Vetterling, W. T. 1988, Numerical Recipes in C (Cambridge: Cambridge Univ. Press), ch. 12
Priestly, M. B. 1981, Spectral Analysis and Time Series, vols. 1, 2 (London: Academic)
Racine, R. 1968, AJ, 73, 233
Rickett, B. J. 1988, in AIP Conf. Proc. 174, Radio Wave Scattering in the Interstellar Medium, ed. J. M. Cordes, B. J. Rickett, & D. C. Backer (New York: AIP), 2
Roy, J.-R., Arsenault, R., & Joncas, G. 1986, ApJ, 300, 624
Roy, J.-R., & Joncas, G. 1985, ApJ, 288, 142
Scalo, J. M. 1984, ApJ, 277, 556
———. 1987, in Interstellar Processes, ed. D. J. Hollenbach & H. A. Thronson (Dordrecht: Reidel), 349

Scalo, J. M., & Miesch, M. S. 1994, in preparation
Spicker, J., & Feitzinger, J. V. 1988a, A&A, 191, 10
———. 1988b, A&A, 191, 186 (SF 1988b)
Spitzer, L. 1978, Physical Processes in the Interstellar Medium (New York: John Wiley)
Tennekes, H., & Lumley, J. L. 1972, A First Course in Turbulence (Cambridge: MIT Press)
Tielens, A. G. G. M., & Hollenbach, D. 1985, ApJ, 291, 722
Townsend, A. A. 1976, The Structure of Turbulent Shear Flow (2d ed.; Cambridge: Cambridge Univ. Press)
Zakharov, V. E., & Sagdeev, R. Z. 1970, Sov. Phys. Dokl, 15, 439
Zel'dovich, Ya. B., Ruzimaikin, A. A., & Sokoloff, D. D. 1983, Magnetic Fields in Astrophysics (New York: Gordon and Breach)
Zeman, O. 1990, Phys. Fluids A, 2, 178
Zurflueh, E. G. 1967, Geophys., 32, 1015